
This manuscript is a preprint and has been formally accepted for publication in **Tectonics**. Subsequent versions of this manuscript may have a slightly different content and the final version will be available via the 'Peer-reviewed Publication DOI' link on the right-hand side of this webpage. Please feel free to contact any of the authors; we welcome feedback

The Impact of Pre-Salt Rift Topography on Salt Tectonics: A Discrete-Element Modelling Approach

*Leonardo M. Pichel^{1,2}, Emma Finch¹, Rob L. Gawthorpe²

¹ School of Earth and Environmental Sciences, University of Manchester, Manchester

² Department of Earth Science, University of Bergen, Bergen, Norway

* *Now at Basins Research Group (BRG), Department of Earth Science and Engineering, Imperial College, Prince Consort Road, London SW7 2BP, UK*

Corresponding author: Leonardo M. Pichel (leonardo.munizpichel@manchester.ac.uk)

Key Points:

- Pre-salt rift structures (horst and tilted blocks) generate base-salt relief acting as a major control on salt deformation
- Variable base-salt slope, step height and connectivity between salt sub-basins affect the kinematics of salt-related deformation
- Models present cross-sectional evolution related to complex structural distribution related to salt flux variations over base-salt relief

Abstract

1 Gravity-driven salt tectonics along passive margins is commonly depicted as
2 comprising domains of updip extension and downdip contraction linked by an
3 intermediate, broadly undeformed zone of translation. This study expands on
4 recently published physical models using discrete-element modelling to demonstrate
5 how salt-related translation over pre-salt rift structures produce complex deformation
6 and distribution of structural styles in translational salt provinces. Rift geometries
7 defined by horsts and tilted fault-blocks generate base-salt relief affecting salt flow,
8 diapirism and overburden deformation. Models show how flow across pairs of tilted
9 fault-blocks and variably-dipping base-salt ramps associated with pre-salt faults and
10 footwalls produce abrupt flux variations that result in alternation of contractional and
11 extensional domains. Translation over tilted fault-blocks defined by basinward-
12 dipping normal faults results in wide, low amplitude inflation zones above footwalls
13 and abrupt subsidence over steep fault-scarps, with reactive diapirs that are
14 squeezed and extrude salt as they move over the fault. Translation over tilted-blocks
15 defined by landward-dipping faults produces narrow inflation zones over steep fault-
16 scarps and overall greater contraction and less diapirism. As salt and cover move
17 downdip, structures translate over different structural domains, being inverted and/or
18 growing asymmetrically. Our models allow, for the first time, a detailed evolution of
19 these systems in cross-section and demonstrate the effects of variable pre-salt relief,
20 salt sub-basin connectivity, width and slope of base-salt ramps. Results are
21 applicable to syn- and post-rift salt basins; ultimately improving understanding of the
22 effects of base-salt relief on salt tectonics and working as a guide for interpretation of
23 complex salt deformation.
24

25

26 **1. Introduction**

27 Gravity-driven salt-related deformation on passive margins is commonly depicted as
28 kinematically-linked domains of updip extension and downdip contraction with an
29 intermediate, broadly undeformed zone of translation (Fig.1a) (Rowan et al., 2000;
30 2004; Hudec and Jackson, 2004, 2007; Brun and Fort, 2011; Quirk et al., 2012;
31 Jackson et al., 2015). More recent studies (Dooley et al., 2017; Dooley and Hudec,
32 2017; Pichel et al., 2018) have shown that this structural zonation represents a
33 simplified view of regional salt tectonics and other factors exert a significant effect on
34 the variability of structures developed in space and time. Salt behaves as a viscous
35 fluid over typical geological strain-rates (e.g. Gemmer et al., 2004; Jackson and
36 Hudec, 2017), and is, therefore, sensitive to the geometry of the surface it flows
37 across (Dooley et al., 2017; 2018; Pichel et al., 2018). As a result, a significant factor
38 influencing the development of salt structures is pre-salt topography (Fig. 1b)
39 (Dooley et al., 2017; 2018; Pichel et al., 2018).

40 Late syn-rift to early post-rift salt basins commonly possess variable salt thickness
41 across base-salt relief as salt is deposited over a topography inherited from a
42 previous rift phase (post-rift salt) or formed during salt deposition (syn-rift salt). In
43 most cases, salt basins are hybrid, with salt being post-rift landward and syn-rift
44 basinward as rifting propagates towards the embryonic oceanic spreading centre,
45 such as in the South and Central Atlantic basins (Rowan 2014; Rowan 2018; Tari et
46 al., 2017). Examples of early post-rift salt basins with significant pre-salt relief include
47 the hydrocarbon-prolific Gulf of Mexico (Peel 1995; Rowan et al., 1995; 2004; Hudec
48 et al., 2013; Dooley and Hudec, 2017) and South Atlantic basins (Mohriak et al.,
49 1995; Hudec and Jackson 2004; Jackson et al., 2008; Davison et al., 2012; Quirk et
50 al., 2012; Jackson et al., 2015a,b). Late syn-rift salt basins, however, e.g. Nova

51 Scotia (Ings and Shimmeld 2006; Albertz et al., 2010; Deptuck and Kendell, 2017),
52 Morocco and Mauritania (Tari et al., 2000; 2003, 2017; Tari and Jabbour, 2013) are
53 associated with more extreme variations of initial salt thickness both within and
54 across grabens (Jackson and Hudec, 2017). Where basement fault throw is larger
55 than salt thickness, salt basins are separated into sub-basins that evolve
56 independently (Jackson and Hudec, 2017). In intermediate scenarios (i.e. late syn-
57 and early post-rift salt), lateral flow between sub-basins occurs but pre-salt
58 topography disrupts and limits downdip translation (Jackson and Hudec, 2017).

59 Early physical models simulated progradation over stepped (Ge et al., 1997) and
60 syn-rift salt basins (Adam and Krezsek, 2012), providing important insights into the
61 effects of differential loading and their structural evolution. These studies, however,
62 did not address the significant effects of early gliding and downdip translation
63 associated with post-rift thermal subsidence and basinward tilting typical of passive
64 margins (Rowan et al., 2004; Peel 2014; Jackson et al., 2014). Recent analogue
65 models (Dooley and Hudec, 2017; Dooley et al., 2017, 2018) have demonstrated
66 how translation across pre-salt relief promotes salt flux variations that result in
67 complex, multiphase salt tectonics and localized zones of deformation (Fig. 1b).
68 These pioneering studies focused on the plan-view evolution and final cross-
69 sectional variations of these systems, not analysing their cross-sectional sequential
70 evolution and variations in diapirism style (i.e. reactive, passive and active,
71 Vendeville and Jackson, 1992a; Hudec and Jackson, 2007) relative to changes in
72 salt flow and overburden deformation patterns.

73 In this study, we employ a Discrete-Element Modelling (DEM) approach (Finch et al.,
74 2003, 2004; Schöpfer et al., 2006; Abe and Urai, 2012; Pichel et al., 2017) to
75 investigate translation across semi-isolated salt sub-basins. These sub-basins are

76 associated with horst and tilted fault-blocks that are realistic base-salt geometries
77 along rifted passive margins. This approach allows for analysis of how salt flux and
78 overburden deformation are affected by: 1) the presence of two pre-salt structures
79 (i.e. tilted fault-blocks), 2) base-salt ramps with different slopes and dip-direction
80 according to the geometry of the underlying pre-salt structures, and 3) variable base-
81 salt step height and connectivity between salt sub-basins. These results are
82 important for understanding the complexity and evolution of salt-related deformation
83 and to guide interpretation of complex salt and supra-salt structures along rifted
84 passive margins and intracratonic salt basins. Furthermore, our results show that salt
85 and supra-salt geometries can be directly linked to pre-salt structures and, therefore,
86 recognition of similar structural patterns on continental margins can aid in the
87 identification of (usually) poorly-imaged pre-salt structures.

88 **2. Method and Models Design**

89 While physical models provide invaluable insight into the 3D geometry, timing and
90 planform sequential evolution of structures (Vendeville and Jackson, 1992; 1995;
91 Dooley et al., 2007; 2015; Ferrer et al., 2012; 2017), they demand a significant
92 amount of time, space and investment (Pichel et al., 2017). Numerical models based
93 on continuum methods, such as finite-element modelling (FEM), have proved very
94 useful in understanding the dynamics of salt flow, allowing more numerical control
95 and realistic stress-strain quantification (Gemmer et al., 2004; Gradmann et al.,
96 2009; Albertz et al., 2010; Weijermars et al., 2015). They are not able, however, to
97 reproduce spontaneous, realistic fault localization and propagation in the cover,
98 which is critical to understand the kinematic and structural style of minibasins and
99 diapirs in areas affected by regional stresses. Thus, FEM cannot reproduce

100 accurately the development of reactive diapirs driven by regional extension
101 (Vendeville and Jackson, 1992a), which are important for the focus of this study.

102 As with any other modelling technique, Discrete-Element Modelling (DEM) has
103 advantages and disadvantages (as discussed in Botter et al., 2014). DEM limitations
104 regard the need of meticulous calibration of particle parameters (Botter et al., 2014)
105 and, because of its discontinuous nature, the (Newtonian) viscous behaviour of salt
106 is approximated (Abe and Urai, 2012; Pichel et al., 2017). Nevertheless, the method
107 allows a good first-order approximation of viscous salt flow at a regional scale that
108 can be used to analyse various aspects of salt tectonics and diapirism driven by
109 regional stresses (Pichel et al., 2017). The advantages of DEM are: 1) scaling is not
110 a restriction; 2) models are easily reproducible, not requiring constant and complex
111 re-meshing; 3) they provide higher resolution and analysis of small-scale
112 deformation within the overburden; and, 4) they promote a more realistic, natural
113 development and evolution of faults and folds in the sedimentary cover than other
114 numerical techniques (Finch et al., 2003; 2004; Pichel et al., 2017). The DEM
115 technique used in this study derives from the Lattice Solid Model (Mora and Place
116 1993, 1994; Place et al. 2002) and the Particle Dynamics Method (Finch et al.,
117 2003). The technique has been extensively applied to model the dynamic evolution
118 of geological systems (Donzé et al., 1994; Place et al., 2002), including faulting and
119 folding processes (Finch et al., 2003, 2004; Schöpfer et al., 2006; Deng et al., 2017;
120 Finch and Gawthorpe, 2017); and viscous flow associated with development of
121 boudinage structures (Abe and Urai, 2012) and salt diapirism (Pichel et al., 2017).

122 The rock mass is treated as an assemblage of circular elements linked by breakable
123 elastic springs through a 'repulsive-attractive' force obeying Newton's Laws of motion
124 (Mora and Place, 1993, 1994; Finch et al., 2004; Hardy and Finch, 2006). The

125 relative strength of each assemblage is defined by its breaking separation, so
126 particles remain bonded until this threshold is exceeded (Donzé et al., 1994; Finch et
127 al., 2004). The motion of particles is assumed to be frictionless and cohesionless
128 with elasto-plastic and ductile behaviour for the overburden and salt, respectively
129 (Finch et al., 2003; Hardy and Finch, 2007, Pichel et al., 2017). The elements have
130 four radii of 0.2, 0.3, 0.4 and 0.5 units and are randomly distributed to reduce failure
131 in preferential orientations within the matrix. A viscous term (v) is added to
132 counteract the elastic behaviour and buildup of kinetic energy within a closed
133 system, enabling its stabilization, which makes it ideal for studying quasi-steady
134 tectonic processes (Finch et al., 2004; Pichel et al., 2017).

135 Forces are resolved in the x and y directions and elements are also subjected to
136 gravitational forces, F_g . The equations that define the inter-relationship of all forces
137 acting on the DEM are:

$$138 \quad F_x = F_{i,n} - v\dot{x} \quad (1)$$

$$139 \quad F_y = F_{i,n} - v\dot{y} + F_g \quad (2)$$

140 Where $F_{i,n}$ corresponds to the total elastic force acting on a particle, v represents the
141 dynamic viscosity and \dot{x} and \dot{y} correspond to the velocity of the particle.

142 In order to make DEM applicable to regional-scale salt tectonics, the properties of
143 elements representing salt are adjusted so they behave macroscopically as a
144 viscous-plastic material. This is achieved by assigning them a negligible breaking
145 separation so their motion is entirely controlled by the viscosity and gravity of the
146 system (Pichel et al., 2017). This does not reproduce the entire range of salt-related
147 mechanical processes; but, based on stress-strain responses obtained by

148 compressional tests (Pichel et al., 2017, fig. 2), works as a good first-order
149 approximation for regional studies. These tests show that a separation threshold of
150 0.001 of particles assigned to salt produces a linear, horizontal response with
151 negligible elastic component. This response is representative of ductile viscous-
152 plastic materials, and notably similar to curves produced by physical (Spiers et al.,
153 1990) and numerical (Li and Urai, 2016) experiments of salt deformation.

154 The model salt viscosity is 1.1×10^9 Pa.s, which is lower than its real viscosity (10^{17} –
155 10^{20} Pa s – Gemmer et al., 2004; Jackson and Hudec, 2017). However, as models of
156 salt flow involve solid-state creep, negligible inertial forces and Reynolds number (Re
157 $\ll 1$), geometric similarity ensures dynamic and kinematic similarity despite
158 numerical parameters not being identical to the real world (Weijermars and
159 Schmeling, 1986; Weijermars et al., 1993; Schultz-Ela et al., 1993; Pichel et al.,
160 2017). The Poisson's ratio (ν) for 2D DEM models is 0.33 and the Young Modulus
161 (E) of the elasto-plastic overburden is of 6.75 GPa. These values are similar to
162 previous studies of salt tectonics (Pichel et al., 2017), and in the range of natural
163 examples of salt and an overburden composed of semi-consolidated siliciclastic
164 rocks or marls (Johnson and DeGraff, 1988; Liang et al., 2007). For a full and more
165 detailed description of scaling of parameters and equations governing DEM, the
166 reader is referred to Mora and Place (1994), Finch et al., (2004); Hardy and Finch
167 (2005, 2006) and Pichel et al., (2017).

168 We present three models where the impact of typical pre-salt rift structures on early-
169 stage salt tectonics, i.e. gliding over a regionally dipping salt detachment (Rowan et
170 al., 2004; Peel 2014b), is tested: i) Model A: horst (Fig. 2a), ii) Model B: tilted fault-
171 blocks with basinward-dipping normal faults (Fig. 2b), and iii) Model C: tilted fault-
172 blocks with landward-dipping normal faults (Fig. 2c). Salt-related gliding and viscous

173 shear drag within the salt are associated with the process of post-rift thermal
174 subsidence and associated margin tilt (e.g. Rowan et al., 2004; Peel 2014; Pichel et
175 al., 2018). These processes are reproduced in the models by simulating salt-related
176 translation over a 3° basinward-dipping salt detachment (Fig. 2), which is in
177 agreement with the slope of salt detachment on passive margins (Tari et al., 2003;
178 Peel 2014) and previous models (Brun and Fort, 2011; Dooley et al., 2007; Dooley et
179 al., 2015; 2017; Pichel et al., 2017).

180 The horst model (A) presents a setting similar to that modelled in Dooley et al.
181 (2017) to illustrate how the approach reproduces the expected kinematics and strain-
182 distribution associated with salt-related translation across pre-salt relief. In addition,
183 we evaluate the sequential evolution of structures in cross-section, something not
184 analysed by Dooley et al. (2017). The model comprises a single central horst (8 km
185 wide and 1.35 km high) defined by a landward- and a basinward-dipping (50°)
186 normal fault at its updip and downdip edges, respectively (Fig. 2a). The tilted fault-
187 block models (B and C) display novel scenarios where we evaluate the influence of
188 steep and gentle base-salt ramps associated with syn-rift normal faults and their
189 footwalls respectively (Fig. 2b-c). These models comprise a pair of equidimensional,
190 10 km wide asymmetric fault-blocks with a 50°-dipping normal fault and a gentle
191 (7.5°) footwall with 1.35 km of maximum structural relief at its crest (Fig. 2b-c, table
192 1). In an additional set of experiments, we evaluate the effects of variable structural
193 relief and connectivity between salt sub-basins by varying the central footwall crest
194 height (Models B1-B4 and C1-C4, fig. 2d-e) (Table 1), while maintaining its location
195 relative to model boundaries.

196 Particles within the salt and overburden are subject to gravitational settling in order
197 to ensure mechanical stability, producing an initial subtle monoclinial relief at the

198 edges of pre-salt structures (Fig. 2). This is caused by preferential flow within the salt
199 driven by the basinward dip of the model immediately prior to overburden translation.
200 The monocline and cover outer-arc extension are also typical geometries associated
201 with end of rift stretching and syn-depositional salt flow (Duffy et al., 2013; Rowan
202 2014; Jackson and Hudec, 2017). For simplicity and general applicability, we do not
203 simulate syn-kinematic sedimentation and assume a homogeneous overburden
204 underlain by a salt interval with densities of, respectively, 2.3 g cm^{-3} and 2.16 g cm^{-3} .
205 These values concur with nature and previous physical and numerical analogues
206 (Gemmer et al., 2005; Ings and Shimmeld, 2006; Dooley et al., 2009, 2012, Albertz
207 and Ings, 2012; Gradmann and Beaumont, 2016). The maximum and minimum salt
208 thicknesses for each model are 2.1 km and 750 m respectively, due to gradual
209 thinning of the salt across pre-salt structural highs. The pre-kinematic overburden
210 has a constant thickness of 0.9 km. As both thickness and density ratios of models
211 and natural examples are similar, stresses in the overburden are dynamically scaled
212 (Weijermars et al., 1993, Pichel et al., 2017). Models are run for 5 million time-steps,
213 which are scaled to 10 Ma in order to simulate translation rates and magnitudes
214 compatible to the early-stage salt-related deformation typical of passive margins
215 (Rowan et al., 2004; Jackson and Hudec, 2005; Peel 2014; Pichel 2018). Thus, a
216 total of 7.5 km of downdip translation is produced by moving model end-walls
217 basinward at an equal and constant rate of 0.75 mm/year, equivalent to a strain-rate
218 in the order of 10^{-16} s^{-1} , within the typical range of salt tectonics along passive
219 margins (Rowan et al., 2004; Jackson and Hudec, 2017; Pichel et al., 2018). The
220 boundaries of the models are not shown because these are not relevant in this
221 study, which focuses on deformation above pre-salt rift structures.

222 **3. Salt flow across a Horst (Model A)**

223 Model A shows that as the salt and overburden move downdip across a pre-salt
224 horst, salt flux variations occur at its edges generating localized zones of
225 deformation that expand through time (Fig. 3). Flux mismatches occur in response to
226 local changes in the cross-sectional area of flow as the entire system moves across
227 the pre-salt rift topography and the associated base-salt ramps. A salt surplus and
228 inflation occur over the landward-dipping normal fault defining the updip edge of the
229 horst; whereas salt deficit and thinning take place over the downdip, basinward-
230 dipping normal fault (Fig. 1b) (c.f. Dooley et al., 2017; 2018). As the salt is originally
231 thicker updip of the horst, the amount of salt being fed towards its updip edge is
232 higher than the amount of salt leaving it, resulting in salt inflation and contraction.
233 Conversely, the amount of salt moving across the downdip edge is significantly less
234 than the amount moving away, producing salt deficit and a monoclinial zone of
235 subsidence that is limited by an extensional hinge at the top of, and a contractional
236 hinge at the base of the basinward-dipping normal fault (Fig. 3) (c.f. Dooley et al.,
237 2017; 2018).

238 During the first 4 Myr, minor salt inflation and cover uplift occur over the updip edge
239 of the horst (Fig. 3a-b). As translation continues and salt gradually thickens, it begins
240 to accelerate and extend as it moves over the gentle and wide basinward-dipping
241 crest of the horst (Fig. 3b). Over its downdip edge, a monoclinial zone of subsidence
242 develops, being defined by extension above the top of, and contraction above the
243 base of the pre-salt basinward-dipping normal fault. The extensional zone is
244 characterized by reactive diapirism and predominantly basinward-dipping listric
245 normal faults in the cover with salt rollers in their footwalls (Fig. 3a-b). The
246 contractional zone is defined by basinward-verging thrusts, salt inflation, cover uplift
247 and folding with outer-arc extension (Fig. 3a-b). During the first 2 Myr, a symmetric

248 reactive diapir (1_R , fig. 3a) forms at the top of the basinward-dipping pre-salt fault
249 where extension is greater (Fig. 3a). In the next 2 Myr, new reactive diapirs (2_R and
250 3_R , fig. 3b) form at this point as the earlier one (1_R , fig. 3b) moves downdip. During
251 this stage (at 4 Myr), an imbrication of thrusts starts to impose differential structural
252 loading driving additional salt attenuation at the base of the pre-salt fault and inflation
253 further downdip (Fig. 3b).

254 With continued downdip translation, salt flux variations are amplified, increasing
255 updip salt inflation and cover uplift, and downdip salt depletion and cover subsidence
256 (Fig. 3c). A broad salt anticline forms over the updip, landward-dipping fault, whereas
257 over the basinward-dipping fault, deformation becomes progressively more complex
258 and inversion of previous structures occurs (Fig. 3b-c). New reactive diapirs (4_R and
259 5_R , fig. 3c) originate at the top of the basinward-dipping fault (i.e. base-salt
260 extensional hinge). Immediately downdip, extensional structures that originally
261 formed near the top of the fault move across a contractional hinge at its base and
262 are inverted (Fig. 3a-c). Normal faults are reactivated as thrusts with minor salt flow
263 in their hangingwall and reactive diapirs (1_R and 2_R , fig. 3b) are squeezed (1_S and 2_S ,
264 fig. 3c).

265 At 8 Myr, continuous inflation over the landward-dipping fault promoted thickening
266 and widening of the salt anticline, which moves partially over the basinward-dipping
267 crest of the horst (Fig. 3d). As a consequence, the anticline undergoes asymmetric,
268 hybrid growth characterized by an active diapir that uplifts and pierces the
269 overburden on the updip limb of the anticline (6_A , fig. 3d); while its downdip limb
270 extends as it glides over the crest of the horst. At the downdip edge of the horst, the
271 wide reactive diapir (4_R , fig. 3d) moves across the basinward-dipping fault, being
272 squeezed and rising further above the contractional hinge (4_S , fig. 3d). Continuous

273 salt depletion over this fault reduces lateral flow and, consequently, a primary weld
274 forms downdip of the horst causing contraction to migrate landward over the pre-salt
275 fault (Fig. 3d).

276 By the end of the model, the broad anticline that initially formed over the landward-
277 dipping fault has translated completely over the crest of the horst (Fig. 3e). This
278 inflated salt body undergoes further extension, being pierced by small reactive
279 diapirs while a new, smaller anticline forms updip, over the landward-dipping fault
280 (Fig. 3e). These geometries and kinematics are similar to the patterns observed in
281 physical models (Fig. 1b) (Dooley et al., 2017). Over the basinward-dipping fault, as
282 salt is dramatically thinned between diapirs (4_S and 7_S , fig. 3e), the two salt sub-
283 basins defined by the horst become partially disconnected. As a consequence, the
284 reactive diapir (5_R , fig. 3d) formed at the top of the fault is squeezed (5_S , fig. 3e) over
285 the earlier formed diapirs resulting in a set of basinward-leaning squeezed diapirs
286 with overturned flanks and, occasionally, secondary welds ($2-4_S$ and 7_S , fig. 3e).

287 **4. Pre-salt Tilted Fault-Blocks with Basinward-dipping Normal Faults (Model** 288 **B)**

289 This model simulates a more complex scenario where salt and overburden
290 translation is affected by a pair of tilted pre-salt fault-blocks (A and B), defining gentle
291 landward-dipping (Footwalls A and B) and steep basinward-dipping base-salt ramps
292 (faults A and B, fig. 2b and 4). Similar to Model A, due to cross-sectional variations of
293 salt flux across base-salt relief, salt inflation and contraction occur above the
294 landward-dipping base-salt ramp, and a monoclinical zone of subsidence and salt
295 depletion limited by extensional and contractional hinges develop over the
296 basinward-dipping base-salt ramp (Fig. 4). However, because of the variable width

297 and dip of these base-salt ramps and their connection with another set of similar
298 structures downdip, flux mismatches and the complexity of deformation are greater.

299 During the first 2 Myr, mild inflation and overburden uplift occurs at the updip edge of
300 Fault-block A (Fig. 4a). The effect is less evident over Fault-block B because
301 basinward movement of the system is partially obstructed by Fault-block A, although
302 deformation above and downdip of Fault B is greater due to an unimpeded
303 basinward advance beyond the fault. There, a 3 km wide zone of extension and
304 reactive diapirism (1_R , fig. 4a) develops over the crest of Fault B, passing into salt
305 thinning and cover subsidence above the fault, and inflation further downdip. From 2
306 to 4 Myr (Fig. 4b), the inflation zone over Footwall A widens and subsidence over
307 Fault B increases. The earlier-formed reactive diapir (1_R , Fault-block B) rises further
308 due to increased extension, and new extensional faults and a reactive diapir (2_R , fig.
309 4b) form immediately updip. In contrast, earlier-formed normal faults are inverted as
310 they move across Fault B (Fig. 4a-b).

311 From 4 to 6 Myr, the inflation/contraction zone associated with Footwall A widens
312 and salt flux variations become greater over Fault A and Footwall B (Fig. 4c). This
313 results in mild subsidence over Fault A with normal faulting at its crest and reverse
314 faults over its base and into Footwall B (Fig. 4c). The first reactive diapir (1_R , fig. 4a-
315 b) emerges and starts to grow passively as it is further extended by moving over the
316 extensional hinge at the crest of Fault B (1_P , Fig. 4c). At the same time, salt
317 continues to thin over Fault B while new thrusts form immediately downdip at its
318 base, where salt flow decelerates (Fig. 4c). By 8 Myr (Fig. 4d), continuous inflation
319 and contraction along Footwall A resulted in the development of two salt anticlines,
320 whereas subsidence and the associated updip extension and downdip contraction
321 are amplified above Fault A. Normal faulting and reactive diapirism occur at the

322 extensional hinge over the crest of the fault, whereas reverse faulting and active
323 diapirism take place at the contractional hinge over the base of the fault, with salt
324 inflation further downdip over Footwall B (Fig. 4d). Over Fault-block B, a wide
325 reactive diapir (3_R , fig. 4d) nucleated at the edge of the previously inflated salt body
326 as it extensionally collapsed when it reached the extensional hinge at the footwall
327 crest of Fault B. The earlier-formed passive and reactive diapirs (1_P and 2_R ,
328 respectively, fig. 4c) moved across this fault and were squeezed and rotated
329 basinward ($1-2_S$, Fig. 4d). The initial diapir (1_S , fig. 4d) became almost completely
330 pinched-off with salt extruding from its crest to produce a small salt sheet (Sh_1 , fig.
331 4d).

332 This abrupt alternation of structural styles led to the development of a hybrid diapir
333 above Fault A (4_H , fig. 4d). The diapir (4_H , fig. 4d) is triangular in shape, being
334 characterized by inward-dipping and younging normal faults and a sub-regional and
335 sub-horizontal extended roof on its updip flank, a geometry characteristic of reactive
336 diapirs formed by extension (*sensu* Vendeville and Jackson, 1992a). Its downdip
337 flank, however, presents a typical upturned and uplifted flap geometry denoting
338 active rise (c.f. Schultz-Ela et al., 1993; Hudec and Jackson, 2007). This indicates
339 that the diapir rose by extension on its updip flank located over the crest of Fault A
340 (e.g. extensional hinge); and by contraction, upturning its downdip flank over the
341 base of the fault (e.g. contractional hinge).

342 By 10 Myr (Fig. 4e), the earlier-formed updip anticline was amplified over Footwall A
343 as it approached its crest (Fig. 4d-e). The intermediate anticline (Fig. 4d) moved over
344 the extensional hinge at the top of Fault A, being unfolded into a monocline and
345 extended by a series of landward-dipping normal faults (Fig. 4e). The earlier-formed
346 hybrid diapir (4_H , fig. 4d) moved across Fault A, rising and upturning its flanks further

347 as it became squeezed over Footwall B (4_S , fig. 4e). The downdip anticline was also
348 further contracted and amplified as it translated over Footwall B (Fig. 4e). A new
349 reactive diapir (6_R , fig. 4e) formed on the downdip limb of this anticline as it reached
350 the extensional hinge above the footwall crest of Fault B. The earlier-formed reactive
351 diapir (3_R , fig. 4d) moved over the contractional hinge at the base of Fault B where it
352 was squeezed and rose further (3_S , fig. 4e). Due to their greater width (1.5-3 km),
353 diapirs 2_S and 3_S did not weld like the oldest, narrower (< 1 km) diapir (1_S , fig. 4e),
354 which remained broadly unchanged as it lost its connection with the source-layer at
355 an earlier stage (Figs 4d-e).

356 **5. Pre-Salt Tilted Fault-Blocks with Landward-dipping Normal Faults (Model** 357 **C)**

358 In this model, Faults A and B define steep base-salt ramps dipping oppositely (i.e.
359 landward) to the flow direction and, thus, act as strong barriers to basinward salt
360 flow, enhancing updip salt inflation and contraction, ultimately, leading to the
361 development of large salt anticlines above them (Fig. 5). The footwalls (A and B) act
362 as gentle and wide basinward-dipping base-salt ramps that locally favour gliding,
363 leading to extension and, particularly over Footwall B, the development of normal
364 faults, reactive diapirs and salt rollers (Fig. 5). Extension is markedly less over
365 Footwall A because it is located between the two landward-dipping faults that
366 obstruct salt flow.

367 From 0-6 Myr (Fig. 5a-c), continuous translation increases salt flux mismatches and
368 inflation over Fault A widening the updip anticline, which moves partially into the
369 footwall crest of Fault A. This produces minor flux variations over Footwall A and,
370 consequently, mild extension of the anticline updip and downdip shortening with the

371 development of a wide zone of inflation as flow is buttressed against Fault B (Fig.
372 5c). By 8 Myr, the zones of inflation over faults A and B are amplified and widened
373 further, being affected by significant outer-arc stretching (Fig. 5d). A reactive diapir
374 (1_R , fig. 5d) forms above the inflated salt over Fault B as this zone expands and
375 begins to be influenced by gliding and extension down Footwall B. The anticline
376 formed over Fault A, however, is only locally extended by outer-arc stresses
377 because downdip translation over Footwall A is buttressed by Fault-block B
378 producing greater inflation and contraction over the entirety of Fault-block A (Fig.
379 5d). By the end of the experiment, both anticlines thicken and widen, extending
380 asymmetrically on their basinward flanks as they move over the extensional hinges
381 on the footwall crest of both faults (Fig. 5e). The anticline above Fault A is
382 asymmetrically extended, with greater extension on its basinward side above
383 Footwall A, and a reactive diapir develops at its crest as it moves beyond Fault A
384 (3_R , fig. 5e). Over Fault-block B, the reactive diapir (1_R , fig. 5e) translates down and
385 away from the footwall crest where it originated, and a new reactive diapir nucleates
386 at that point (2_R , fig. 5e).

387 **6. Effects of step height and connectivity between sub-basins**

388 In this set of experiments, we test the effects of pre-salt structural relief and the
389 associated variable salt thickness and connectivity across sub-basins defined by
390 basinward- and landward-dipping normal faults by varying the height of the central
391 footwall-crest (Table 1, figs. 2d-e, 6a-d and 7a-d). In the models with the largest
392 structural relief (models B4 and C4, table 1, figs. 6d and 7d), there is no salt over the
393 footwall crest so the sub-basins are initially disconnected.

394 In both cases of sub-basins, salt flux mismatches are driven by and directly
395 proportional to the base-salt relief and associated salt thickness contrasts across
396 sub-basins. For basinward-dipping pre-salt normal faults (Fig. 6), an increase in the
397 footwall crest height results in greater buttressing and salt inflation over the footwall
398 (i.e. base-salt landward-dipping ramp), and greater salt thinning and cover
399 subsidence above the fault (i.e. base-salt basinward-dipping ramp) (Fig. 6a-c). Flux
400 mismatches are, therefore, enhanced where salt is thinner over fault crests (Fig. 6).
401 The magnitude and width of inflation increase progressively as the height of the
402 footwall crest increases (from 1.2 to 2.1 km, fig. 6a-d). As cover subsidence and salt
403 thinning are also intensified over the larger normal fault scarps, the width of
404 associated extensional and contractional zones, the number of normal faults, and
405 intensity of reactive diapirism also increase (Fig. 6a-c). The locus of maximum
406 subsidence remains closer to the base of the fault scarp as the pre-salt step height
407 increases and, consequently, the connectivity between sub-basins decreases (Fig.
408 6).

409 These relationships do not completely apply where salt sub-basins either side of the
410 normal fault were initially disconnected due to greater pre-salt topography. In this
411 scenario, extension and contraction are more localized, and marked salt attenuation
412 and welding occurs over the fault (Fig. 6d). A narrow zone of extension forms due to
413 gliding and salt thinning over the fault, which passes immediately downdip to a wider
414 area of contraction above the base of the fault and into the downdip fault-block (Fig.
415 6d). A salt sheet advances over the footwall crest from the updip sub-basin over
416 thinned salt of the downdip sub-basin, developing another set of extensional and
417 contractional structures above it (Fig 6d). Gradual translation and inflation over the
418 footwall crest allows the salt to build enough gravitational instability, causing it to

419 advance basinward by thrusting over the extensionally thinned salt in the downdip
420 sub-basin (Fig. 6d). Once the salt advances over the downdip sub-basin, however,
421 these initially isolated systems no longer evolve independently as the sheet and its
422 roof impose additional structural loading onto the downdip sub-basin, amplifying salt
423 expulsion over the border fault and inflation further downdip (Fig. 6d).

424 In landward-dipping pre-salt normal fault systems, the base-salt relief associated
425 with the fault dips steeply and in the opposite direction to the salt flow, therefore,
426 acting as a strong barrier to downdip translation (Fig. 7). As a result, the magnitude
427 of salt inflation, overburden contraction and uplift is larger for greater faults (Fig. 7a-
428 c), except in the case of disconnected sub-basins (Fig. 7d). The observed zone of
429 inflation is located progressively landward as footwall crest height increases,
430 because the salt has greater difficulty flowing across higher relief steps, remaining
431 pinned above them for a longer time (Fig. 7a-d). As a result, fewer and smaller
432 reactive diapirs nucleate over the inflated salt for models with higher footwall crests
433 (Fig. 7a-c). In a similar way to the basinward-dipping faults model (Fig. 6), when the
434 salt sub-basins are initially isolated they evolve independently until the salt inflates
435 enough above the footwall crest that it becomes able to advance by thrusting
436 basinward over previously thinned strata in the downdip sub-basin (Fig. 7d).

437 **7. Discussion**

438 **7.1. Effects of Pre-salt Rift Geometries on Salt Flow and Overburden** 439 **Deformation**

440 The horst model (Model A) reproduces a similar dynamic evolution and distribution of
441 structural styles to the physical models of Dooley et al. (2017; 2018) (Figs. 1b, 8a
442 and 9a). Translation and the associated variations in the cross-sectional area of flow

443 across a pre-salt horst result in salt inflation over the updip edge of the horst and salt
444 thinning over its downdip edge (Fig. 8a and 9a). A salt anticline forms over the updip
445 edge of the horst and, as it progressively thickens and widens, it moves onto the
446 crest of the horst where it collapses and extends (Figs. 3 and 8a). In contrast, over
447 its downdip, basinward-dipping edge, a monoclinial zone of subsidence develops and
448 is characterized by extension and reactive diapirism above the pre-salt footwall crest,
449 and contraction and diapir squeezing at the base of the pre-salt fault (Figs. 3 and
450 8a).

451 Tilted fault-block models (Figs. 4-7) demonstrate how translation across sets of
452 steep and gentle base-salt ramps associated with syn-rift normal faults and footwalls
453 result in more complex patterns of overburden deformation and diapirism. This
454 occurs because the salt flux varies more frequently and abruptly as it is influenced by
455 greater changes in base-salt relief (Fig. 8b-c and 9b-c).

456 In models where salt and overburden translate across tilted fault-blocks defined by
457 basinward-dipping normal faults (Model B, figs. 4 and 8b), wide zones of salt inflation
458 and overburden contraction develop over the gentle landward-dipping base-salt
459 ramps above their footwalls (Figs. 8b and 9b). This occurs because initial salt
460 thickness decreases towards the footwall crest and, with downdip translation, the
461 cross-sectional area of salt arriving at that point is larger than that leaving (Fig. 9b).
462 Conversely, the cross-sectional area of salt leaving the basinward-dipping normal
463 fault is greater than that arriving at its footwall crest, which generates a monoclinial
464 zone of subsidence over the fault defined by extension above its crest and
465 contraction over its base (Figs. 4, 8b and 9b). This structural style is similar to that
466 developed downdip of the horst (Model A), but it is narrower and more complex due
467 to the influence of adjacent oppositely-dipping base-salt ramps (Figs. 8a-b). As

468 translation continues, deformation intensifies with the zones of extension and
469 contraction expanding landward and basinward respectively (Fig. 4). Salt anticlines
470 developed above the footwall translate over the footwall crest and become extended
471 and pierced by reactive diapirs (Figs. 4 and 8b). Extensional structures (i.e. normal
472 faults and reactive diapirs) initially formed near the footwall crest (i.e. extensional
473 hinge) translate over the base of the fault scarp where flow decelerates (i.e.
474 contractional hinge), and are rotated, inverted, and/or squeezed (Figs. 4, 8b and 9b).
475 This pattern repeats for each fault-block encountered resulting in more abrupt
476 transitions, overlap and alternation of contractional and extensional domains relative
477 to settings without or with simpler base-salt relief, e.g. horst blocks (Fig. 8a-b).

478 Where tilted fault-blocks are defined by landward-dipping normal faults (Model C),
479 intense obstruction of salt flow and, thus, greater salt inflation and contraction are
480 observed against and above the normal fault (Figs. 5, 8c and 9c). This results in
481 higher-amplitude, but narrower zones of inflation and contraction compared with the
482 basinward-dipping normal fault model (Figs. 8b-c). Additionally, the presence and
483 proximity of two barriers to basinward salt flow associated with the underlying
484 landward-dipping faults results in overall greater magnitudes of shortening and
485 reduced extension and subsidence between the two fault blocks when compared to
486 the other models (Figs. 8 and 9). As translation continues, salt anticlines become
487 progressively wider and thicker, eventually moving across the footwall crest and over
488 the gentle basinward-dipping footwall (Figs. 5 and 8c). As a consequence, the
489 anticlines are asymmetrically extended and pierced by reactive diapirs, with greater
490 extension occurring on their downdip limb over the basinward-dipping footwalls (Fig.
491 5 and 8c). However, as regional contraction does not favour diapirism as much as
492 extension (Vendeville and Jackson, 1992a; 1994), translation over pre-salt fault-

493 blocks defined by landward-dipping normal faults results in considerably less
494 diapirism than in other settings (Fig. 5 and 8).

495 Our experiments confirm the hypothesis that pre-salt structures and base-salt
496 topography are responsible for nucleating salt structures by promoting changes in
497 salt flow and overburden deformation patterns (Ge et al., 1997; Dooley et al., 2017;
498 2018; Deptuck and Kendell, 2017; Pichel et al., 2018) (Figs. 3-5). As translation
499 progresses, salt and overburden structures eventually leave the pre-salt topography
500 where they originated and are reactivated downdip by the next pre-salt structure
501 encountered (Figs. 3-5). These early-formed structures act as weakness zones that
502 may be eventually exploited and amplified by later processes such as loading or
503 tectonic reactivation, further complicating the evolution of these systems and our
504 ability to interpret them (Dooley et al., 2018).

505 The models presented here reproduce a wide range of diapirism styles (i.e. reactive,
506 passive and active, Hudec and Jackson 2007) (Figs. 3-5, 8 and 10a-b), along with
507 small salt sheets formed by extrusion and thrusting (Figs. 4, 6 and 10b). Positioning
508 of a salt structure over distinct base-salt domains results in complex, hybrid diapir
509 growth in which one of its flank undergoes extension while the other is in contraction
510 (Figs. 3-5, 10c-d). This occurs because the salt structure (i.e. diapir or anticline) is
511 simultaneously influenced by contrasting flux variations and, thus, velocity
512 mismatches (c.f. Dooley et al., 2017), and variable stress regimes on its flanks when
513 these are located over distinct base-salt domains. Anticlines inflate over base-salt
514 landward-dipping ramps whilst being asymmetrically extended and pierced by
515 reactive diapirs over basinward-dipping ramps (anticline over Fault-block B in fig. 4d-
516 e and updip anticlines in figs. 3, 5 and 10d). Conversely, a diapir rises by extension
517 over the footwall crest of basinward-dipping faults whilst actively piercing and

518 upturning its roof above the base of the fault (hybrid diapir, fig. 4d and 10c). This
519 phenomenon has been briefly described in an area of thick salt and prominent base-
520 salt relief in the Santos Basin (Pichel et al., 2018), and may also be recognized over
521 allochthonous salt in the Gulf of Mexico (Duffy and Peel pers. comm. 2018).

522 Salt flux variations and associated overburden deformation are driven primarily by
523 shear-drag within the salt (i.e. Couette-flow, c.f. Dooley et al., 2017; Pichel et al.,
524 2018), a process also illustrated in dynamic models based on our experiments (Fig.
525 9a-c). Earlier numerical simulations reproducing viscous salt drag and overburden
526 translation (SaltDragON, Peel[®]) exhibit remarkably similar kinematics associated
527 with simpler flat-ramp systems (Pichel et al., 2018). These earlier models accurately
528 simulate salt flux variations, sedimentation and development of asymmetric
529 minibasins, i.e. ramp-syncline basins (Pichel et al., 2018), but do not reproduce
530 lateral overburden deformation (i.e. extension and contraction) nor diapirism. The
531 models presented here complement this earlier work by showing the effects of non-
532 uniform translation over complex base-salt relief, with resultant overburden
533 contractional and extensional deformation (i.e. folding, faulting) and diapirism. These
534 are, nonetheless, simplifications of salt flow in nature, which is typically hybrid and
535 simultaneously affected by varying proportions of Couette and Poiseuille flow
536 components (Rowan et al., 2004; Weijermars et al., 2014; Pichel et al., 2018).

537 Variable pre-salt structural relief and sub-basin connectivity have a significant impact
538 on flow kinematics and overburden deformation. Higher pre-salt fault topography and
539 associated differences in salt thickness across neighbouring sub-basins produce
540 stronger buttressing, flux variations and flow disruptions. This produces greater
541 updip inflation and contraction over landward-dipping base-salt ramps, and greater
542 downdip subsidence and associated extension and contraction over basinward-

543 dipping base-salt ramps (Figs. 6-7). In cases where sub-basins are initially
544 disconnected, they evolve independently until inflated salt from the updip fault-block
545 is able to advance basinward into the downdip fault-block by thrusting (Fig. 6d and
546 7d). In these cases, the final observed distribution of extensional and contractional
547 strain is more localized and repeated on each sub-basin (Figs. 6d and 7d). The width
548 and magnitude of localized strain provinces is proportional to the width and
549 steepness of the base-salt ramps that they are associated with (Figs. 4-8). Steep
550 and narrow ramps, which in our models are associated with normal fault scarps,
551 result in stronger, more abrupt salt flux changes and deformation over a narrower
552 region. Gentle and wider ramps, associated with footwall dip-slopes, produce
553 deformation that is subtler, but distributed over a wider area (Figs. 4-8).

554 **7.2. Applicability and Comparison with Seismic Examples**

555 The models have limitations associated with free-edge effects and moving
556 boundaries (c.f. Hardy and Finch, 2005; Pichel et al., 2017). Small-scale structures
557 and the degree of faulting might differ locally from natural examples as these are
558 affected by other variables not modelled here, e.g. changes in sedimentation pattern,
559 loading, intra-salt stratigraphy, and tectonic reactivation. Nonetheless, our models
560 produce salt flux variations, diapirism and distribution of structural styles similar to
561 most recent physical experiments (Dooley et al., 2017; 2018) (compare fig. 1b and
562 8a), and examples of syn- and post-rift salt basins (Figs 11 and 12). The benefits of
563 using DEM to model translation and salt flux variations over significantly variable
564 base-salt topography are that results are easily reproducible and afford analysis of
565 the sequential evolution of highly-strained systems and diapirs in cross-section. This
566 is crucial to understand the distribution of salt and overburden geometries that
567 undergo a complex, multiphase history of extension and contraction. Discrete-

568 element models (DEM) cannot substitute finite-element models (FEM) or physical
569 models as these methods have other advantages; but the DEM technique applied
570 here complements these other approaches improving the understanding of regional
571 salt tectonics.

572 Results presented here are especially applicable to late syn-rift salt basins, which
573 are mainly affected by thin-skinned salt tectonics and present wedge-shaped salt
574 sequences across half-grabens (Rowan 2014; Jackson and Hudec, 2017). Examples
575 of these basins include Nova Scotia (Fig. 11) (Albertz and Ings, 2010; Deptuck and
576 Kendall; 2017), offshore Morocco, Mauritania (Davison 2005; Tari and Jabbour,
577 2013; Tari et al., 2017) and the Red Sea (Mitchell et al 2010; Rowan 2014).
578 Additionally, initial basin geometries used in these models can also be applicable to
579 segments of post-rift salt basins where significant base-salt topography is inherited
580 from previous phases of rifting. Examples include Santos (Fig. 12) (Davison et al.,
581 2012; Pichel et al., 2018); Campos (Davison et al., 2012; Dooley et al., 2017),
582 Kwanza and Lower Congo (Hudec and Jackson 2004; Jackson and Hudec, 2005;
583 Peel 2014); and Gulf of Mexico (Hudec et al., 2013; Dooley and Hudec, 2017).

584 As seen in examples of syn-rift salt from Nova Scotia, at the top of pre-salt faults and
585 footwalls that define basinward-dipping base-salt ramps, deformation is
586 characterized by extension (i.e. salt rollers and normal faults, fig. 11). Conversely, at
587 the base of basinward-dipping faults and/or over landward-dipping faults or footwalls,
588 deformation is characterized by salt inflation and contraction, which are evidenced by
589 fault inversion and thrusting (Fig. 11a), and diapir squeezing (Fig. 11b).

590 In the case of post-rift salt in the Santos Basin, variations of base-salt relief are less
591 pronounced, but the strain and structural style distribution are remarkably similar to

592 the models presented here (Fig. 12). Salt anticlines form by contraction (indicated by
593 intra-salt seaward-vergent shear zones) above landward-dipping base-salt ramps,
594 and are later asymmetrically extended by basinward-dipping normal faults above a
595 broadly flat base-salt high (Fig. 12a-b). Deformation over most of this horst is
596 dominated by extension and widening of earlier salt anticlines, and reactive diapirs
597 characterized by a triangular shape and inward-dipping and younging normal faults
598 (Fig. 12a-c). Minor later inflation occurred as structures approached a subtle
599 landward-dipping base-salt ramp near the horst margin as indicated by an earlier
600 reactive diapir that later uplifts a broadly tabular roof (Fig. 12c). Above the large
601 basinward-dipping base-salt ramp defined by a set of basinward-dipping normal
602 faults, deformation is characterized by a monoclinial zone of subsidence (Fig. 12a).
603 This zone of subsidence is characterized by updip extension and downdip
604 contraction similar to models presented here (Fig. 9 and 12). An earlier salt anticline
605 is extended at the crest of this ramp (Fig 12d), while a fold-thrust belt develops at
606 and downdip of its base (Fig. 12e).

607 Models simulating variable base-salt ramp height (Figs. 7-8) help to understand
608 along-strike variations of salt-related structural styles on rifted margins due to
609 variability in the pre-salt rift geometry associated with normal fault throw,
610 segmentation, spacing and polarity (Fig. 13). An increase of throw towards the
611 centre of basinward-dipping faults results in greater inflation over the footwalls and
612 subsidence above the faults with, consequently, greater extension at the footwall
613 crest and contraction at the base of the fault (Fig. 13a). Thus, greater base-salt relief,
614 usually near the centre of syn-rift faults, can produce increased salt rise and
615 diapirism (Fig. 13a), whereas towards the fault tips, structures tend to be more subtle
616 and dominated by salt subsidence and inflated anticlines (Fig. 13b). Closely spaced

617 fault-blocks generate more abrupt flux variations, depending on the base-salt relief
618 they generate. For closely spaced, basinward-dipping fault blocks, there is an
619 increase in the buttressing effect at the base of the fault and against the landward-
620 dipping footwall, amplifying contraction and squeezing of earlier structures (left-hand
621 side, Fig. 13a). Buttressing and contraction are also increased in the case of
622 reversed fault polarity (i.e. landward-dipping faults) producing larger salt anticlines
623 but, due to less extension of the overburden, less diapirism than above basinward-
624 dipping faults (c.f. fig. 13a and c).

625 **8. Conclusions**

626 The models presented here reproduce salt flux variations and structural styles
627 associated with salt and overburden translation across pre-salt topography that are
628 similar to recent physical experiments (c.f. Dooley et al., 2017; 2018). Our numerical
629 modelling results complement and expand on these previous studies by investigating
630 the cross-sectional sequential evolution and multiphase diapirism in these settings,
631 and testing the influence of a more complex and realistic pre-salt structural
632 framework of connected variably-dipping base-salt ramps. These models do not
633 intend to simulate the entire lateral extent and temporal evolution of salt basins,
634 rather they focus on illustrating how pre-salt relief nucleates salt structures and
635 influences their evolution by disrupting early salt flow.

636 Base-salt ramps with variable slopes related to tilted fault-blocks and their bounding
637 normal faults produce higher-frequency variation of structural styles and diapirism
638 than in simpler flat-ramp base-salt systems defined by pre-salt horsts. As salt and
639 cover move downdip, structures translate over contrasting structural domains, being
640 inverted and/or growing asymmetrically. Gliding over tilted-blocks defined by

641 basinward-dipping normal faults produces wide, low amplitude zones of inflation
642 above footwalls, and abrupt, narrow zones of subsidence over steep fault-scarps.
643 Reactive diapirs form near the footwall crest, and become squeezed, potentially
644 extruding salt sheets as they move across the fault. Translation over tilted-blocks
645 defined by landward-dipping faults produces narrow zones of inflation over the steep
646 fault-scarp, with overall greater contraction and less diapirism as flow is obstructed
647 by ramps dipping contrary to flow direction. Results also demonstrate how variable
648 height, dip and orientation of pre-salt structures play a key role on the evolution of
649 these systems and can partially explain along-strike variation of salt-related
650 deformation in rifted margins.

651 The modelled geometries and distribution of structural styles are comparable to
652 seismic examples of both syn- and post-rift salt basins where prominent base-salt
653 relief exists. Additionally, the models show an important component of asymmetric
654 diapir growth across contrasting base-salt geometries observed in modern, high-
655 resolution 3D-seismic data. Ultimately, results of this study improve our
656 understanding of how pre-salt structures impact salt flow, overburden deformation
657 and distribution of structural styles along rifted passive margins; and work as a guide
658 to the interpretation of complex diapir geometries and their link with pre-salt
659 structures.

660 **Acknowledgments**

661 We wish to thank Christopher Jackson, Frank Peel, Jonathan Redfern, Tim Dooley
662 and Oliver Duffy for sharing their insights and for fruitful discussions. We also thank
663 the constructive reviews and criticism of Tim Dooley and Juan Soto, who significantly
664 contributed to improve this manuscript and Luc Lavier for the excellent editorial

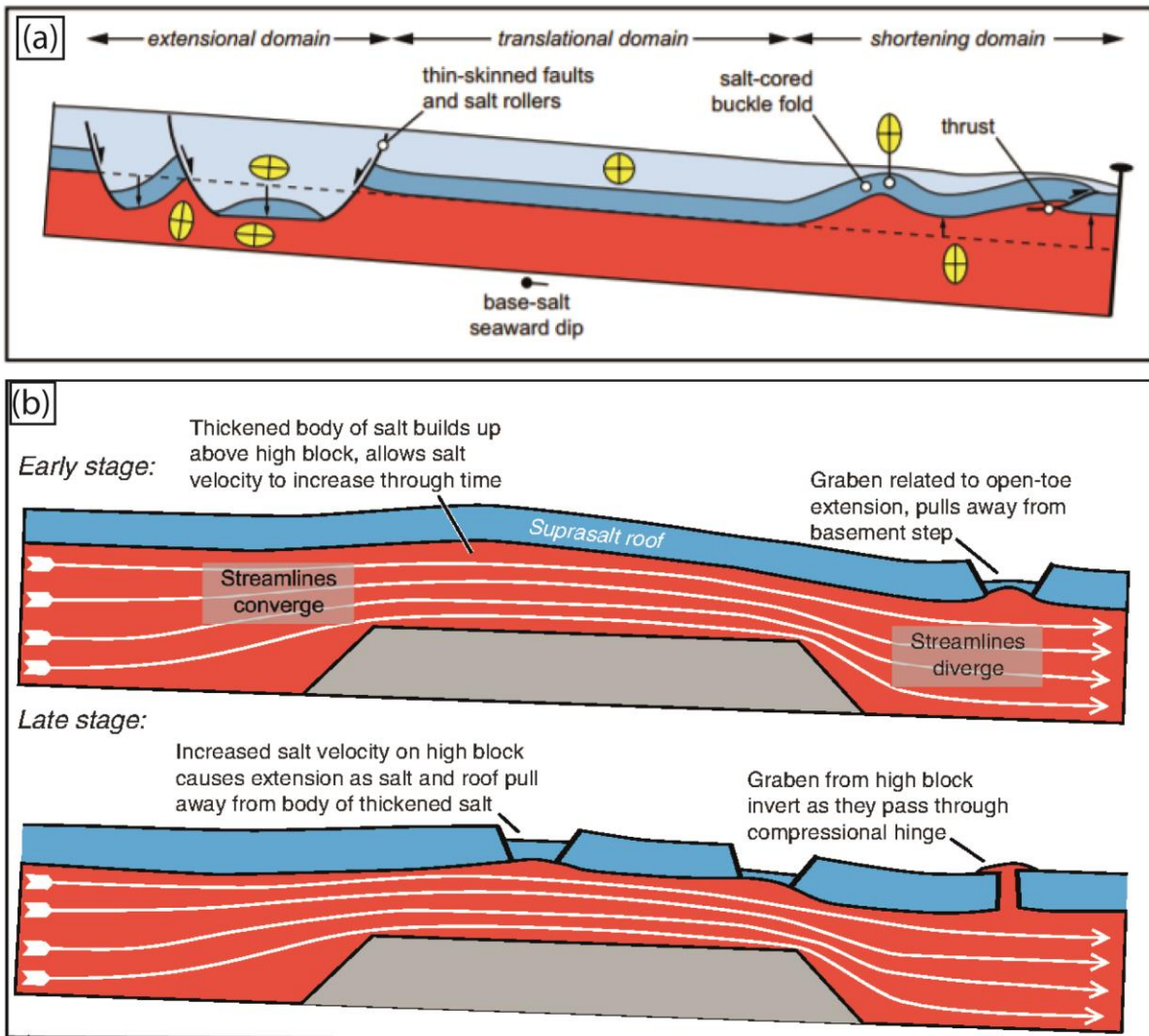
665 handling. We thank CGG for providing access to 3D seismic dataset and the section
 666 presented from the Santos Basin. The first author would like to thank the Science
 667 without Borders program and CNPq, Brazil for sponsoring his PhD research. The
 668 North Africa Research Group (University of Manchester) and its sponsors are also
 669 acknowledged for providing substantial support during the main author's PhD. We
 670 also thank the Norwegian Academy of Science and Letters VISTA program for
 671 funding Gawthorpe's VISTA Professorship and the first author's visiting position at
 672 the University of Bergen where most of this research was conducted. The modelling
 673 data can be obtained from the link:

674 [https://www.researchgate.net/publication/329844061_Discrete-](https://www.researchgate.net/publication/329844061_Discrete-Element_Modeling_data_of_salt-related_translation_over_pre-salt_rift_structures)
 675 [Element_Modeling_data_of_salt-related_translation_over_pre-salt_rift_structures.](https://www.researchgate.net/publication/329844061_Discrete-Element_Modeling_data_of_salt-related_translation_over_pre-salt_rift_structures)

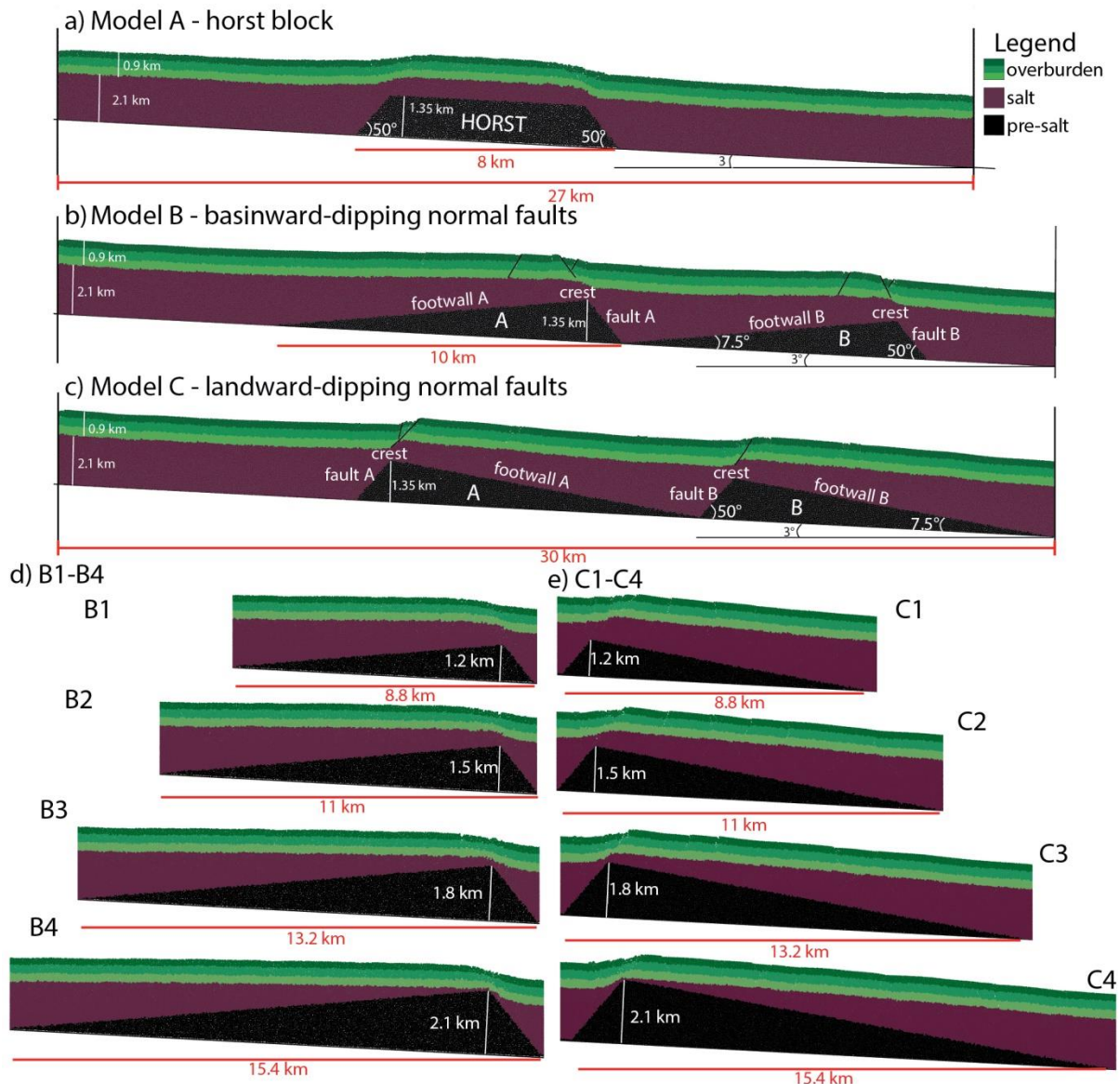
676 **Figures and Table Captions**

	pre-salt faults dip-direction	block length (km)	step height (km)	min salt thickness (km)
Model A	land and basinward	8	1.35	0.75
Model B	basinward	10	1.35	0.75
Model C	landward	10	1.35	0.75
Model B1	basinward	8.8	1.2	0.9
Model B2	basinward	11	1.5	0.6
Model B3	basinward	13.2	1.8	0.3
Model B4	basinward	15.4	2.1	0
Model C1	landward	8.8	1.2	0.9
Model C2	landward	11	1.5	0.6
Model C3	landward	13.2	1.8	0.3
Model C4	landward	15.4	2.1	0

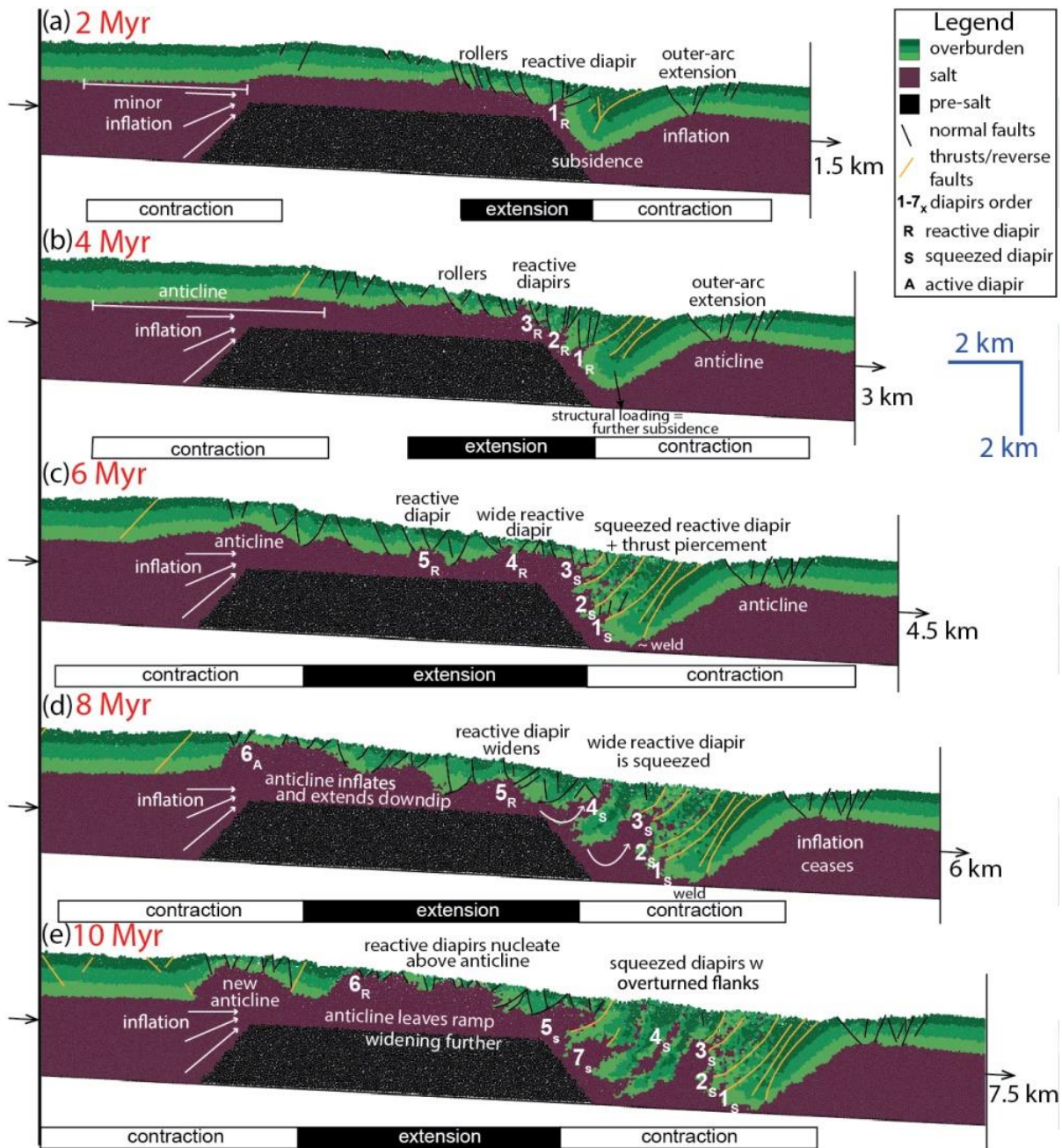
677 Table 1: Summary of variable input parameters for all models.
 678



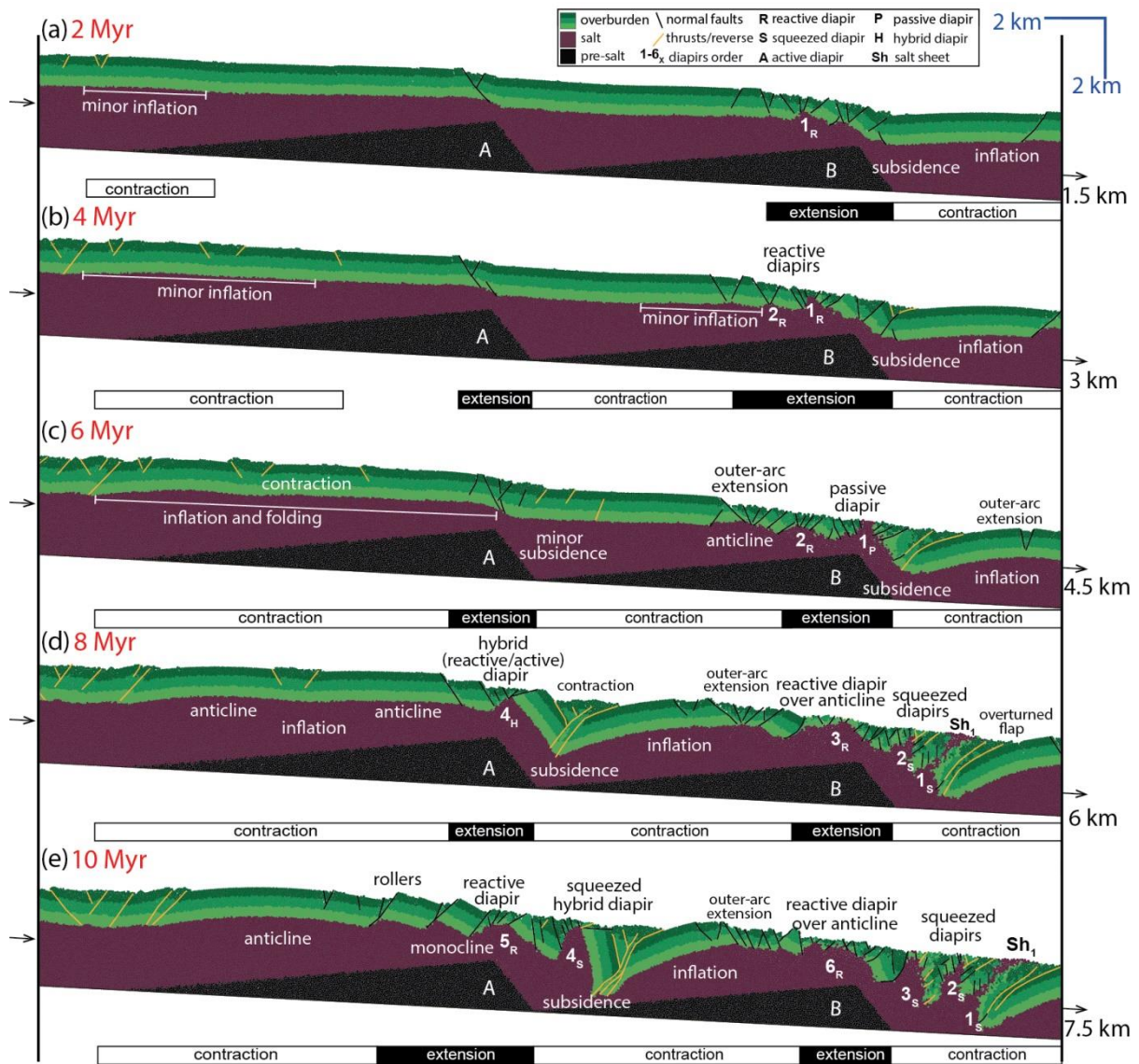
679
 680 Figure 1: (a) Classical distribution of regional salt tectonics structural domains in passive
 681 margins: updip extensional and downdip contractional domains kinematically linked by an
 682 undeformed translational province (from Jackson et al., 2015). (b) Kinematic model based on
 683 recent physical models showing effects of salt-related translation across pre-salt topography
 684 and consequent variations of salt flux (streamlines) resulting in complex deformation history
 685 and localized zones of deformation. These are characterized by salt inflation followed by
 686 extensional collapse over the updip edge of the horst; and a monoclinial zone of subsidence
 687 limited by updip extension and downdip contraction over its downdip edge (from Dooley et
 688 al., 2017).



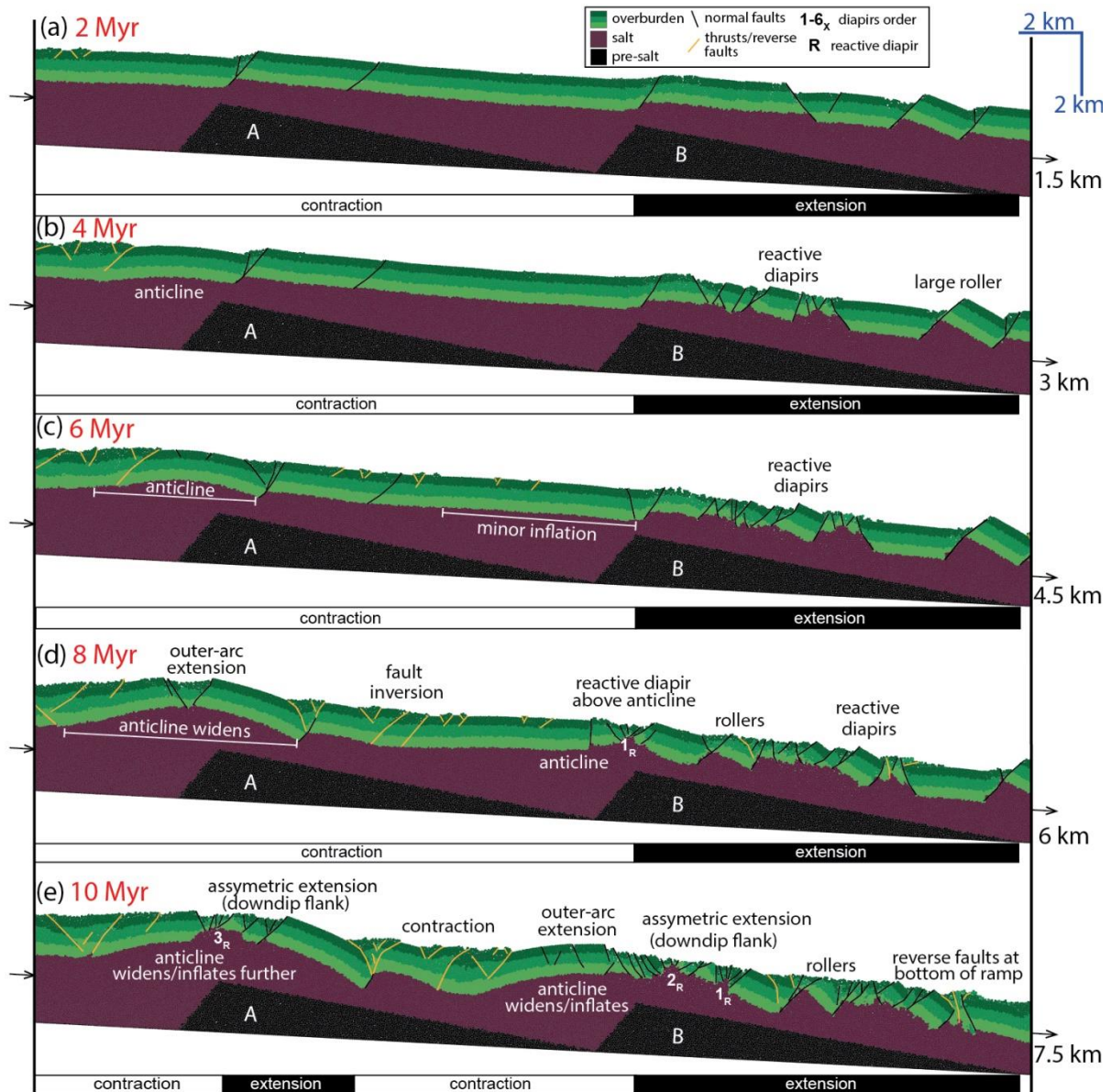
689
 690 Figure 2: Initial model designs, dimensions and thicknesses after a phase of particle settling
 691 for the main experiments presented in this study: (a) Model A: horst; (b) Model B: basinward-
 692 dipping normal faults; (c) Model C: landward-dipping normal faults; (d) focused views
 693 showing variation of structural relief and salt connectivity for basinward-dipping normal faults
 694 (Models B1-B4); and (e) for landward-dipping normal faults (Models C1-C4). The modelled
 695 media consists of a box with free walls and rigid, undeformable pre-salt structures (black).
 696 The models have an initial thickness of 3 km, with the salt section (magenta) having a
 697 maximum thickness of 2.1 km and minimum thickness over the footwall crest decreasing as
 698 the structural relief increases for models B1-B4 and C1-C4, with no salt over the footwall
 699 crest of models B4 and C4. The pre-kinematic overburden (green) has constant thickness of
 700 900 m.
 701



702
 703 Figure 3: Sequential evolution shown in increments of 2 Ma (a-e) of Model A: Horst, which
 704 simulates translation over a single pre-salt horst and consequent salt flux variations across a
 705 simple base-salt topography. Model edges are not shown to improve visualization of relevant
 706 structures at the centre of the model. As the system translates, structures move over
 707 different structural domains, being reactivated and/or inverted. These extensional (black box)
 708 and contractional (white boxes) domains shift over time. Diapirs are represented by numbers
 709 1-7 and their corresponding style of growth is indicated in subscript.
 710

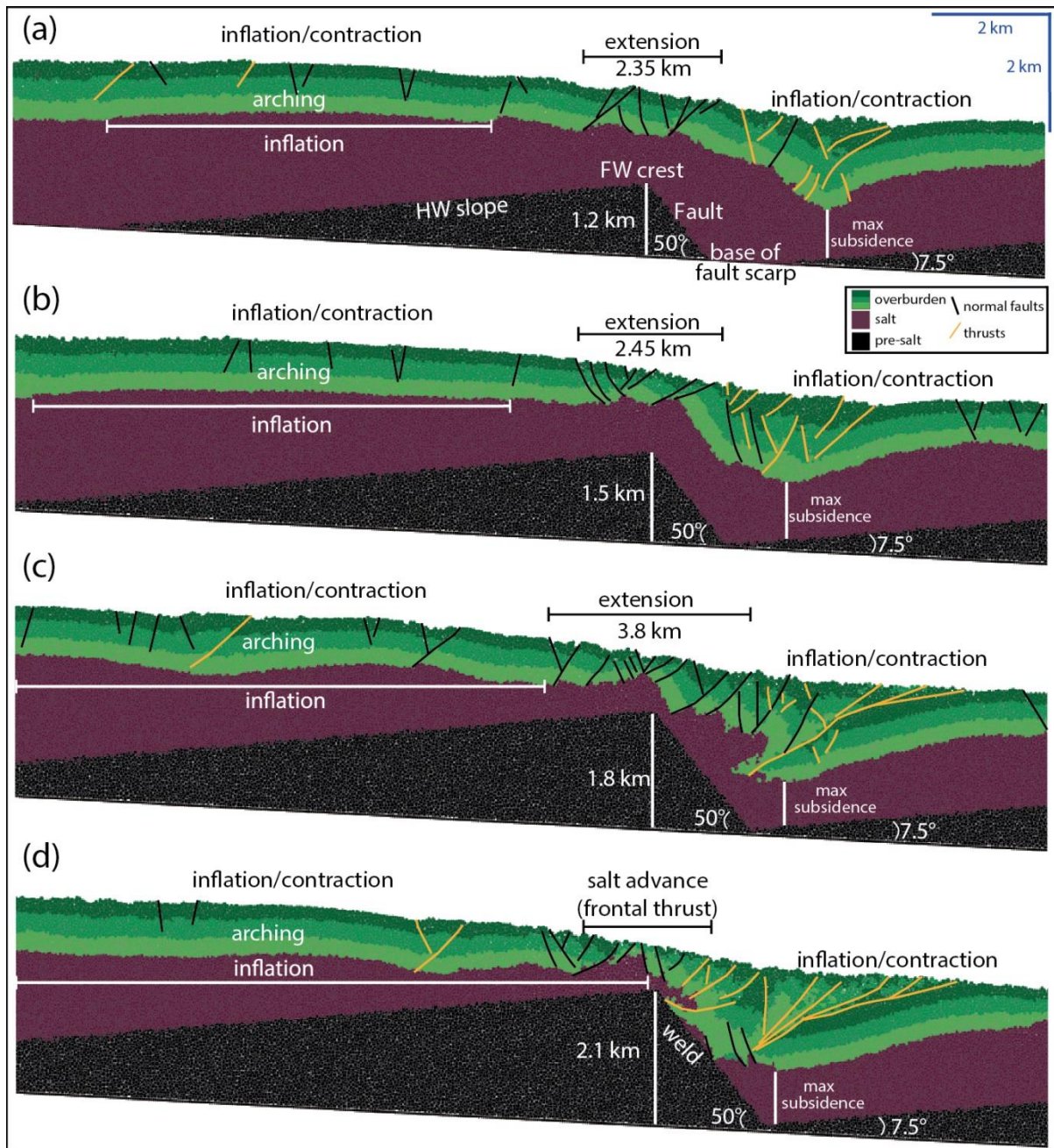


711
 712 Figure 4: Sequential evolution shown in increments of 2 Ma (a-e) of Model B: Basinward-
 713 dipping Normal Faults, simulating translation over tilted fault-blocks (A and B). Each of these
 714 blocks defines a gentle landward-dipping base-salt ramp and a steep basinward-dipping
 715 base-salt ramp. To improve visualization of relevant structures only the centre of the model
 716 is shown. Salt flux variations occur above each ramp segment complicating flow kinematics
 717 and overburden deformation. As the system translates, structures move over different
 718 structural domains, being reactivated and/or inverted. Extensional (black boxes) and
 719 contractional (white boxes) domains occur over each fault-block, which change through time.
 720 Diapirs are represented by numbers 1-6 and their corresponding style of growth in subscript.
 721 A salt sheet (S_1) forms due to diapir squeezing at the bottom of the distal basinward-dipping
 722 ramp.
 723

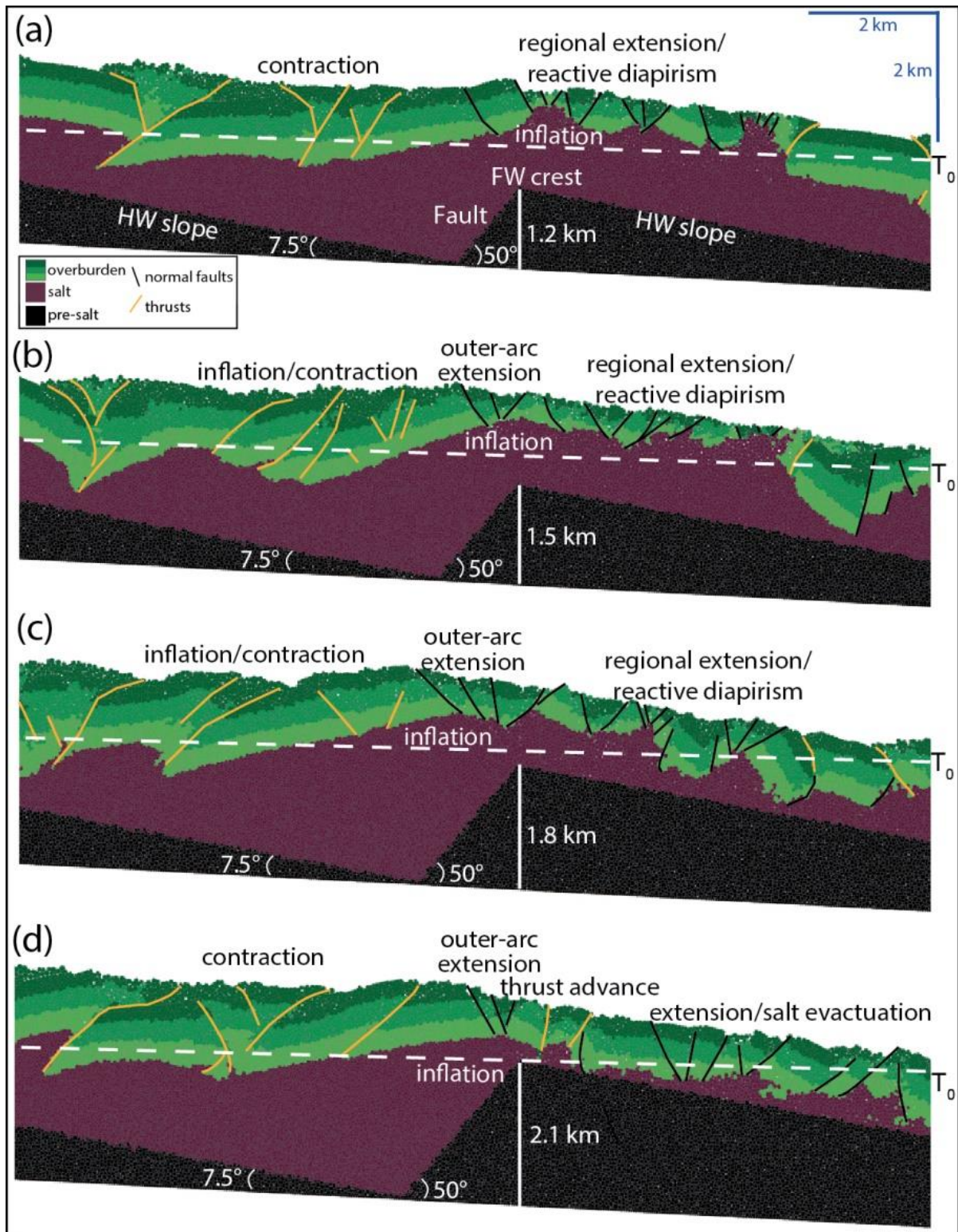


724
 725
 726
 727
 728
 729
 730
 731
 732

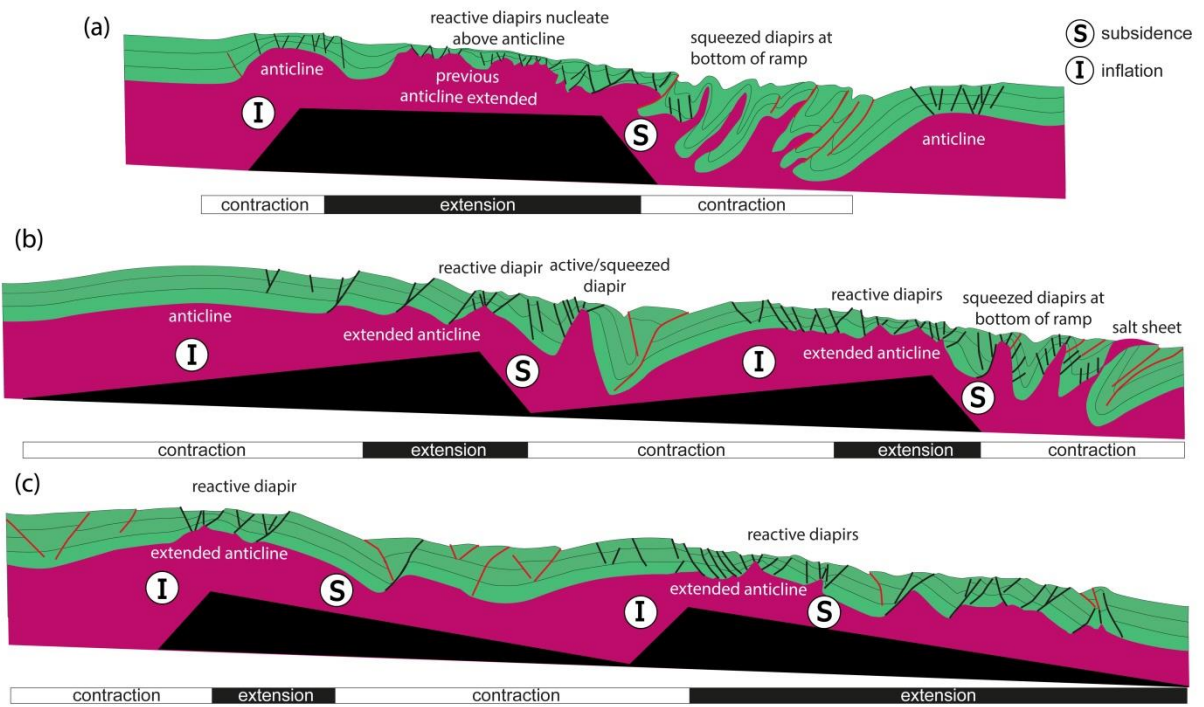
Figure 5: Sequential evolution presented in increments of 2 Ma (a-e) of Model C: Landward-dipping Normal Faults, which simulates salt-detached translation over a pair of tilted fault-blocks defining steep landward-dipping base-salt ramps updip and gentle basinward-dipping base-salt ramps downdip. To improve visualization of relevant structures at the centre of the model, its edges are not shown. Contractional (lower white boxes) domains and extensional (lower black boxes) occur over each half-graben by the end of the experiment. Diapirs are represented by numbers 1-3 and their corresponding style of growth in subscripted letters.



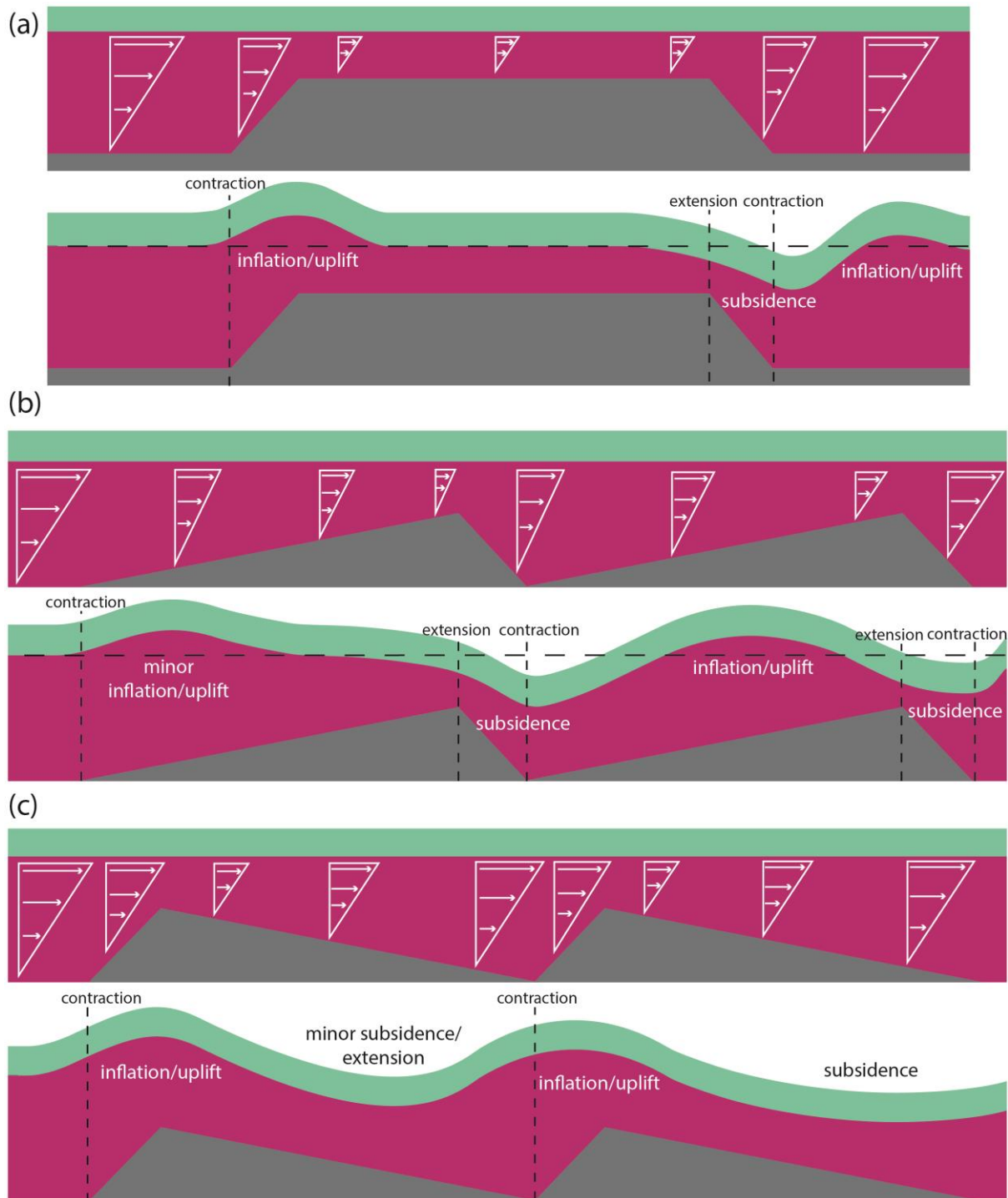
733
 734 Figure 6: Final results (after 10 Myr) showing the effects of salt connectivity and pre-salt step
 735 height on lateral salt flow, diapirism and overburden deformation for tilted fault-blocks
 736 defined by basinward-dipping faults: (a) B1, (b) B2, (c) B3, and (d) B4. Maximum salt
 737 thickness in all models is 2.1 km at the deepest portion of the graben and minimum salt
 738 thickness is of 900 m (B1), 600 m (B2), 300 m (B3) and 0 m (B4) over the pre-salt structural
 739 highs. Model boundaries are far from the section of the model shown so structures are not
 740 affected by boundary artefacts. Zones of updip inflation are shown by white horizontal
 741 and zones of extension by black horizontal. Normal faults are in black and reverse faults in
 742 orange.
 743



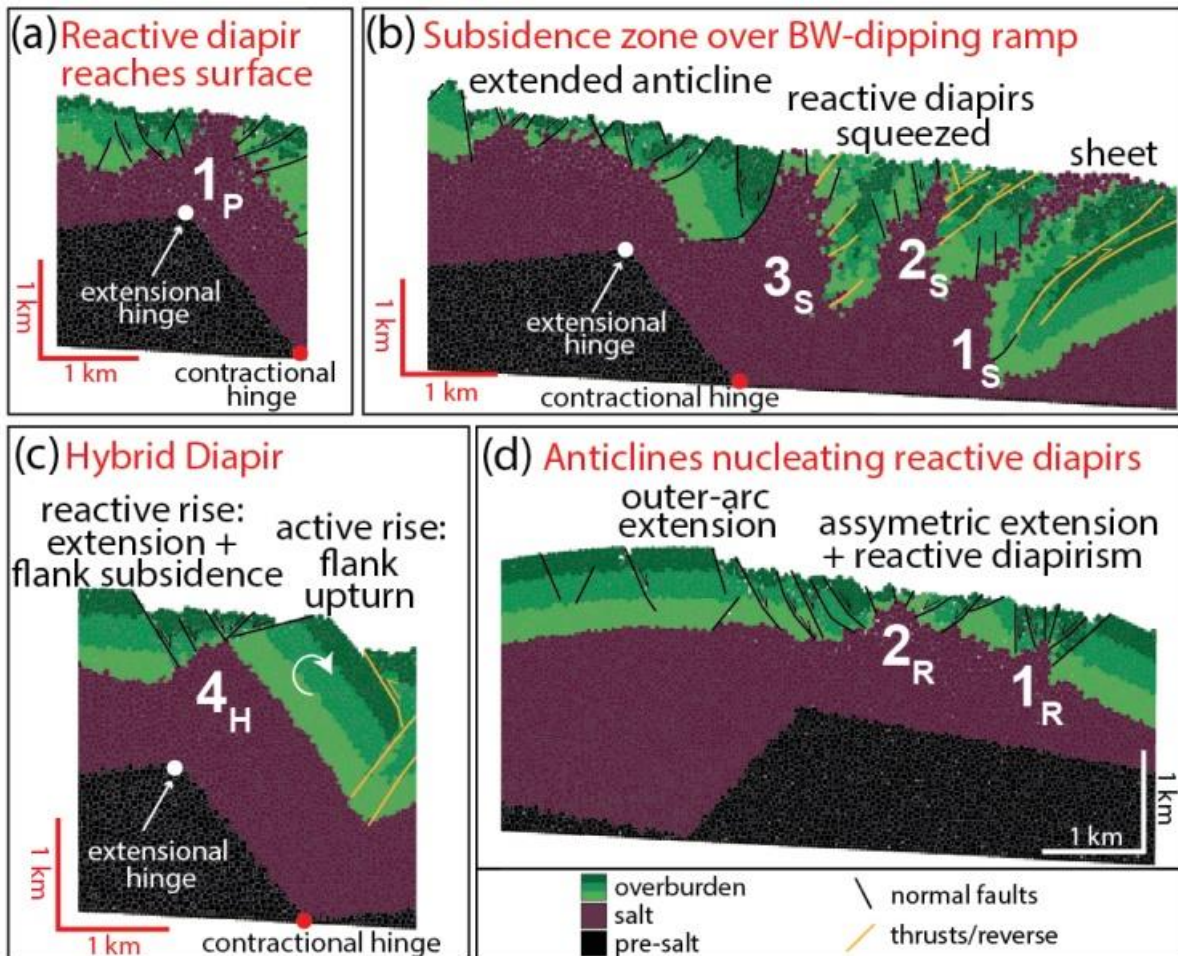
744
 745 Figure 7: Final (after 10 Myr) results showing the effects of salt connectivity and pre-salt step
 746 height on lateral salt flow, diapirism and overburden deformation for tilted fault-blocks
 747 defined by landward-dipping faults: (a) C1, (b) C2, (c) C3, and (d) C4. Maximum salt
 748 thickness in all models is 2.1 km at the deepest portion of the graben and minimum salt
 749 thickness is of 900 m (B1), 600 m (B2), 300 m (B3) and 0 m (B4) over the pre-salt structural
 750 highs. White dashed-lines represent original top salt (T_0). Model boundaries are far from the
 751 section of the model shown so structures are not affected by boundary artefacts. Zones of
 752 inflation are indicated by white dashed lines. Normal faults are in black and reverse faults in
 753 orange.



754
 755 Figure 8: Synthesis diagram of final model results comparing structural style distribution
 756 associated with (a) a pre-salt horst, and pairs of tilted fault-blocks defined by (b) basinward-
 757 dipping and (c) landward-dipping pre-salt rift faults. (S) indicates zones of subsidence and (I)
 758 zones of inflation and contraction. The distribution of structural domains is shown at the
 759 bottom of each section with extensional domains in black boxes and contractional domains
 760 in white boxes. Normal faults are shown in black and reverse faults in red. Pre-salt rift
 761 structures are in black, salt in pink and overburden in light green.

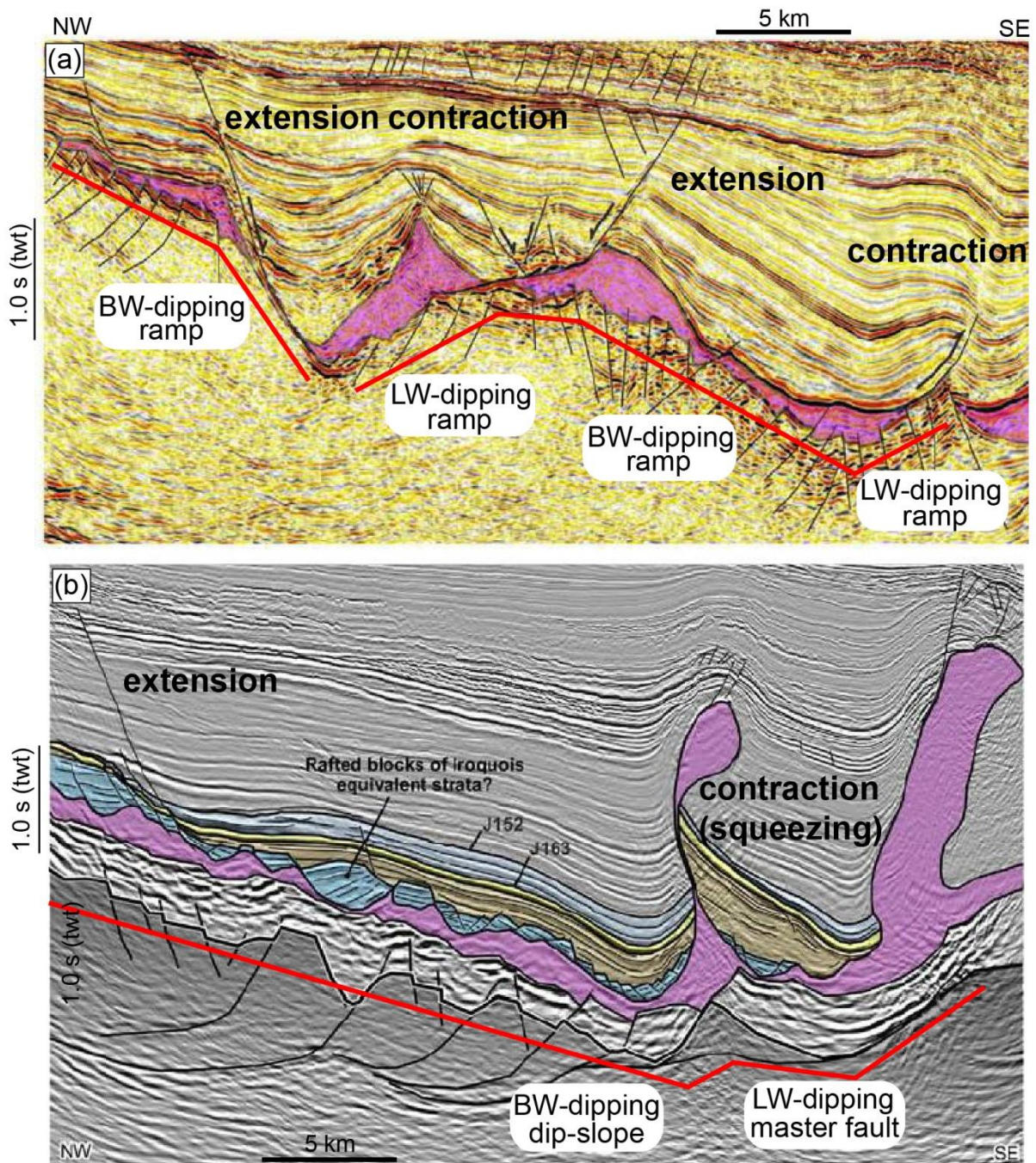


762
 763 Figure 9: Simplified diagram based on model results illustrating initial salt structures and the
 764 dynamics of viscous shear (Couette salt flow) and flow perturbations related to gliding and
 765 salt flux changes due to variations in original salt thickness across pre-salt topography: (a)
 766 pre-salt horst; and pairs of tilted fault-blocks defined by (b) basinward-dipping and (c)
 767 landward-dipping pre-salt rift faults.
 768

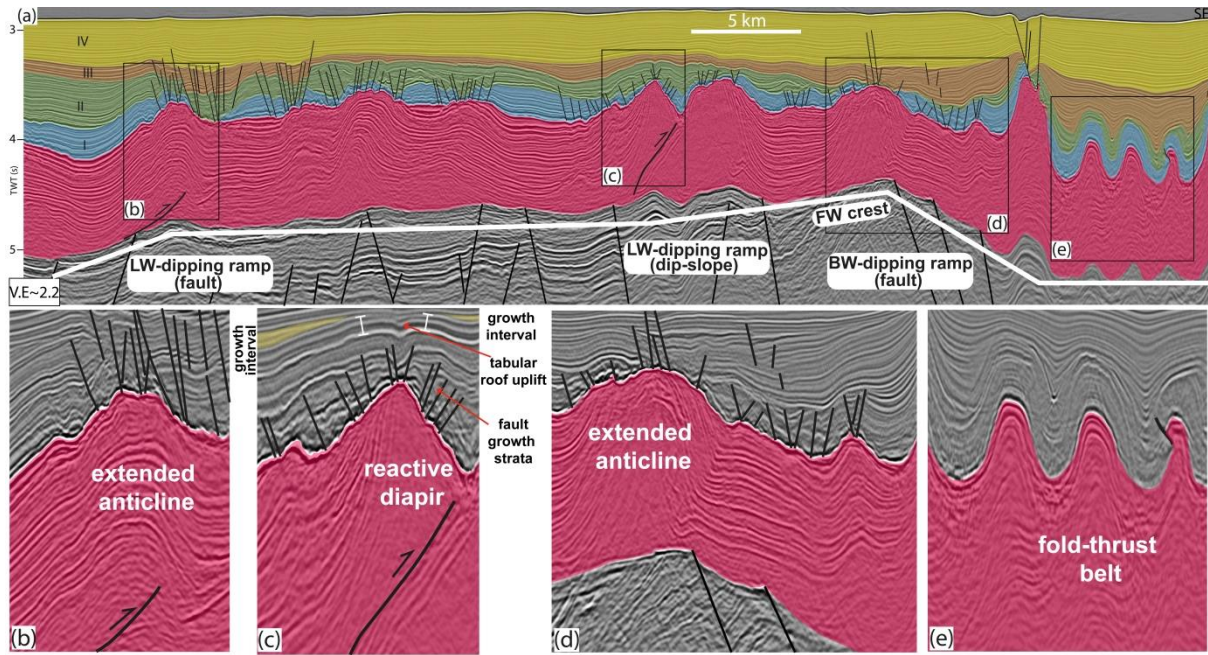


769
 770
 771
 772
 773
 774
 775
 776
 777
 778
 779
 780
 781
 782

Figure 10: Focused sections showing examples of salt response and complex, multiphase styles of diapirism associated with flow over base-salt ramps. (a) After continuous extension, a reactive (i.e. extensional) diapir reaches the surface and continues to evolve as a passive diapir (1_P) at an extensional hinge at the crest of a basinward-dipping normal fault of Model B (4 Myr). (b) Reactive diapirs are squeezed (1_S, 2_S and 3_S) and normal faults inverted as they move over the base of the basinward-dipping (BW) fault (contractional hinge) with salt sheet extruding from the crest of the basinwardmost diapir (1_S) in Model B (10 Myr). (c) Hybrid diapir characterized by extension and reactive rise over the footwall crest (extensional hinge) and active diapirism and flank upturn over the base of the fault (contractional hinge) in Model B (8 Myr). (d) Salt anticline inflates over a landward-dipping fault whilst its downdip flank collapses, being extended and pierced by reactive diapirs over the basinward-dipping dip-slope in Model C (10 Myr).

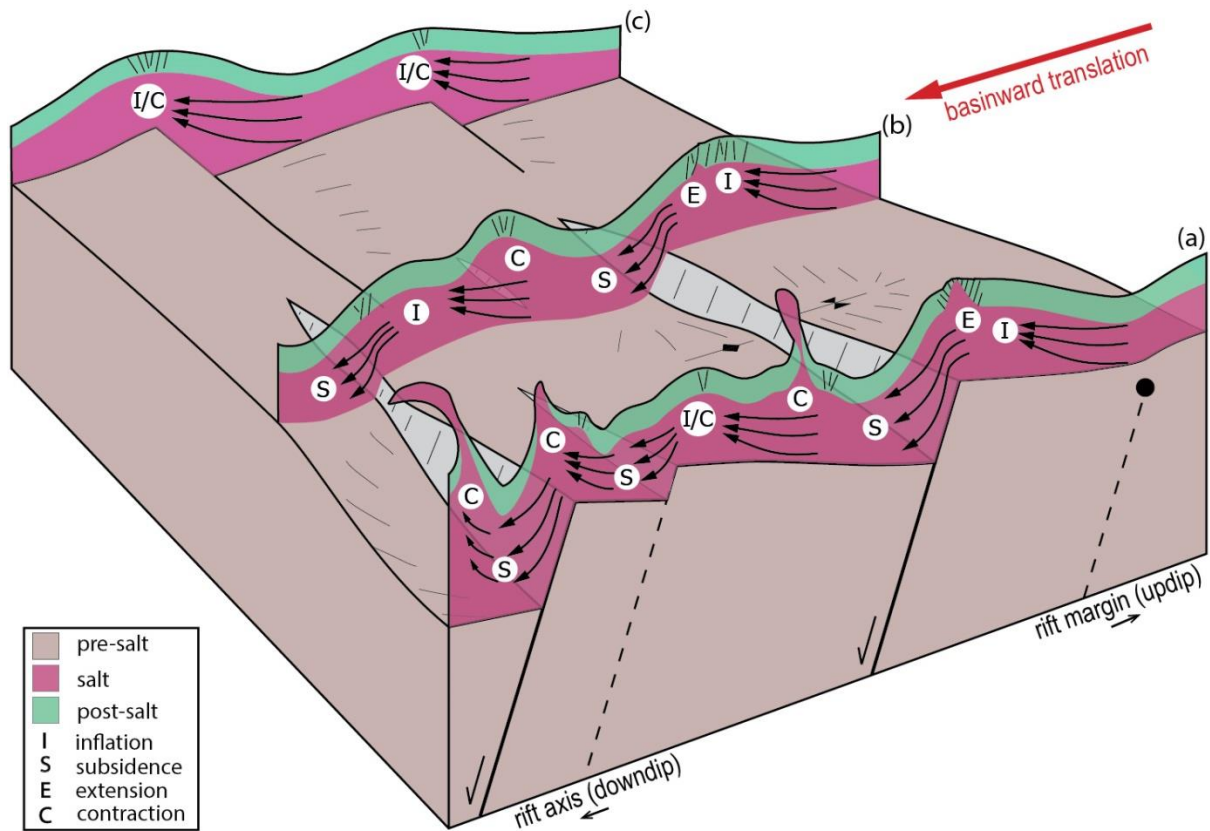


783
 784 Figure 11: Seismic examples of the impact of complex pre-salt syn-rift topography on salt
 785 tectonics of a late syn-rift salt basin in Nova Scotia (modified from Deptuck and Kendell,
 786 2017). (a) Movement over a pair of steep basinward- (BW) and landward (LW)-dipping
 787 ramps produces extension at the top of the basinward-dipping ramp and simultaneous
 788 contraction and uplift at its bottom and over the landward-dipping ramp. Further downdip,
 789 another zone of extension and salt expulsion occurs at the top of a gentle basinward-dipping
 790 step while a previous extensional minibasin is translated basinward, being contracted at the
 791 bottom of this ramp and over a small landward-dipping step. (b) Extension occurs at the top
 792 of a gentle basinward-dipping ramp; while a previously reactive/passive diapir formed further
 793 updip is squeezed as it is buttressed against a steep landward-dipping pre-salt step. Red
 794 lines below salt interval indicate the large-scale base-salt geometries.
 795



796
 797
 798
 799
 800
 801
 802
 803
 804
 805
 806
 807
 808

Figure 12: (a) High-resolution regional seismic section illustrating the effects of complex pre-salt relief on salt flow in a post-rift salt basin, Santos Basin, Brazil. Salt is on average 2 km thick and has a prominent intra-salt layering, which works as kinematic indicator. (b)-(e) Close-ups. (b) Movement over a landward-dipping base-salt step results in contraction (evidenced by basinward-vergent intra-salt shear zone) and development of a salt anticline that is asymmetrically extended above the base-salt high. Over the pre-salt horst, deformation is driven mainly by extension and reactive diapirism. (c) Close-up of reactive diapir shows growth strata associated to normal faults and later uplift of a tabular roof with growth strata in yellow. At the downdip edge of the tilted fault-block, movement over the pre-salt footwall crest (FW crest) and basinward-dipping fault produces a zone of extension at the top (d) and contraction (fold-thrust-belt) at its base (e).



809
 810 Figure 13: Along-strike variation of salt structural domains linked to pre-salt rift topography
 811 associated with fault segmentation, throw variations and dip polarity typical of rift settings (rift
 812 template based on Gawthorpe and Leeder, 2000). Profile (a) shows variations related to
 813 high-relief as well as closely-spaced basinward-dipping rift faults, whereas profile (b)
 814 illustrates variations associated with low-relief basinward-dipping faults and profile (c)
 815 landward-dipping faults.

816 **References**

817 Abe, S., & Urai, J. L. (2012). Discrete element modeling of boudinage: Insights on
 818 rock rheology, matrix flow, and evolution of geometry. *Journal of Geophysical*
 819 *Research: Solid Earth*, 117(B1). <https://doi.org/10.1029/2011JB008555>

820 Adam, J., & Krézsek, C. (2012). Basin-scale salt tectonic processes of the
 821 Laurentian Basin, Eastern Canada: insights from integrated regional 2D seismic
 822 interpretation and 4D physical experiments. *Geological Society, London, Special*
 823 *Publications*, 363, 331-360. <https://doi.org/10.1144/SP363.15>

824 Albertz, M., Beaumont, C., Shimeld, J. W., Ings, S. J., & Gradmann, S. (2010). An
 825 investigation of salt tectonic structural styles in the Scotian Basin, offshore Atlantic

826 Canada: 1. Comparison of observations with geometrically simple numerical
827 models. *Tectonics*, 29(4). <https://doi.org/10.1029/2009TC002539>

828 Allen, M. P., Tildesley, D. J. (1987). *Molecular Simulation of Liquids*. Clarendon,
829 Oxford.

830 Botter, C., Cardozo, N., Hardy, S., Lecomte, I., & Escalona, A. (2014). From
831 mechanical modeling to seismic imaging of faults: A synthetic workflow to study the
832 impact of faults on seismic. *Marine and Petroleum Geology*, 57, 187-207.
833 <https://doi.org/10.1016/j.marpetgeo.2014.05.013>

834 Brun, J. P., & Fort, X. (2011). Salt tectonics at passive margins: Geology versus
835 models. *Marine and Petroleum Geology*, 28(6), 1123-1145.
836 <https://doi.org/10.1016/j.marpetgeo.2011.03.004>

837 Davison, I., (2005). Central Atlantic margin basins of North West Africa: geology and
838 hydrocarbon potential (Morocco to Guinea). *Journal of African Earth Sciences*, 43(1),
839 254-274. <https://doi.org/10.1016/j.jafrearsci.2005.07.018>

840 Davison, I., Anderson, L., & Nuttall, P., (2012). Salt deposition, loading and gravity
841 drainage in the Campos and Santos salt basins. *Geological Society, London, Special*
842 *Publications*, 363, 159-174. <https://doi.org/10.1144/SP363.8>

843 Deng, C., Gawthorpe, R. L., Finch, E., & Fossen, H. (2017). Influence of a pre-
844 existing basement weakness on normal fault growth during oblique extension:
845 Insights from discrete element modeling. *Journal of Structural Geology*, 105, 44-61.
846 <https://doi.org/10.1016/j.jsg.2017.11.005>

847 Deptuck, M. E., & Kendell, K. L. (2017). A review of Mesozoic-Cenozoic Salt
848 Tectonics Along the Scotian Margin, Eastern Canada. In: Soto, J. I., Flinch, J., &

849 Tari, G. (Eds.). (2017). Permo-Triassic Salt Provinces of Europe, North Africa and
850 the Atlantic Margins: Tectonics and Hydrocarbon Potential. Elsevier, 287-312.
851 <https://doi.org/10.1016/B978-0-12-809417-4.00014-8>

852 Donzé, F., Mora, P., & Magnier, S. A., (1994). Numerical simulation of faults and
853 shear zones. *Geophysical Journal International*, 116(1), 46-52.
854 <https://doi.org/10.1111/j.1365-246X.1994.tb02126.x>

855 Dooley, T. P., Jackson, M., & Hudec, M. R., (2007). Initiation and growth of salt-
856 based thrust belts on passive margins: results from physical models. *Basin*
857 *Research*, 19(1), 165-177. <https://doi.org/10.1111/j.1365-2117.2007.00317.x>

858 Dooley, T. P., Jackson, M. P., & Hudec, M. R., (2009). Inflation and deflation of
859 deeply buried salt stocks during lateral shortening. *Journal of Structural*
860 *Geology*, 31(6), 582-600. <https://doi.org/10.1016/j.jsg.2009.03.013>

861 Dooley, T. P., Hudec, M. R., & Jackson, M. P., (2012). The structure and evolution of
862 sutures in allochthonous salt. *AAPG bulletin*, 96(6), 1045-1070.
863 <https://doi.org/10.1306/09231111036>

864 Dooley, T. P., Jackson, M. P. A., & Hudec, M. R., (2015). Breakout of squeezed
865 stocks: dispersal of roof fragments, source of extrusive salt and interaction with
866 regional thrust faults. *Basin Research*, 27(1), 3-25. <https://doi.org/10.1111/bre.12056>

867 Dooley, T. P., Hudec, M. R., Carruthers, D., Jackson, M. P., & Luo, G., (2017). The
868 effects of base-salt relief on salt flow and suprasalt deformation patterns—Part 1:
869 Flow across simple steps in the base of salt. *Interpretation*, 5(1), SD1-SD23.
870 <https://doi.org/10.1190/INT-2016-0087.1>

871 Dooley, T. P., & Hudec, M. R. (2017). The effects of base-salt relief on salt flow and
872 suprasalt deformation patterns—Part 2: Application to the eastern Gulf of Mexico.
873 Interpretation, 5(1), SD25-SD38. <https://doi.org/10.1190/INT-2016-0088.1>

874 Duffy, O. B., Gawthorpe, R. L., Docherty, M., & Brocklehurst, S. H. (2013). Mobile
875 evaporite controls on the structural style and evolution of rift basins: Danish Central
876 Graben, North Sea. Basin Research, 25(3), 310-330.
877 <https://doi.org/10.1111/bre.12000>

878 Ferrer, O., Jackson, M. P. A., Roca, E., & Rubinat, M., (2012). Evolution of salt
879 structures during extension and inversion of the Offshore Parentis Basin (Eastern
880 Bay of Biscay). Geological Society, London, Special Publications, 363, 361-380.
881 <https://doi.org/10.1144/SP363.16>

882 Ferrer, O., McClay, K., & Sellier, N. C., (2017). Influence of fault geometries and
883 mechanical anisotropies on the growth and inversion of hanging-wall synclinal
884 basins: insights from sandbox models and natural examples. Geological Society,
885 London, Special Publications, 439, 487-509. <https://doi.org/10.1144/SP439.8>

886 Finch, E., Hardy, S., & Gawthorpe, R., (2003). Discrete element modelling of
887 contractional fault-propagation folding above rigid basement fault blocks. Journal of
888 Structural Geology, 25(4), 515-528. [https://doi.org/10.1016/S0191-8141\(02\)00053-6](https://doi.org/10.1016/S0191-8141(02)00053-6)

889 Finch, E., Hardy, S., & Gawthorpe, R., (2004). Discrete-element modelling of
890 extensional fault-propagation folding above rigid basement fault blocks. Basin
891 Research, 16(4), 467-488. <https://doi.org/10.1111/j.1365-2117.2004.00241.x>

892 Finch, E., & Gawthorpe, R., (2017). Growth and interaction of normal faults and fault
893 network evolution in rifts: insights from three-dimensional discrete element

894 modelling. Geological Society, London, Special Publications, 439, SP439-23.
895 <https://doi.org/10.1144/SP439.23>

896 Gawthorpe, R. L., & Leeder, M. R. (2000). Tectono-sedimentary evolution of active
897 extensional basins. Basin Research, 12(3-4), 195-218.
898 <https://doi.org/10.1111/j.1365-2117.2000.00121.x>

899 Ge, H., Jackson, M. P., & Vendeville, B. C., (1997). Kinematics and dynamics of salt
900 tectonics driven by progradation. AAPG Bulletin, 81(3), 398-423.

901 Gemmer, L., Ings, S. J., Medvedev, S., & Beaumont, C., (2004). Salt tectonics driven
902 by differential sediment loading: stability analysis and finite-element
903 experiments. Basin Research, 16(2), 199-218. <https://doi.org/10.1111/j.1365-2117.2004.00229.x>

904

905 Gemmer, L., Beaumont, C., & Ings, S. J., (2005). Dynamic modelling of passive
906 margin salt tectonics: effects of water loading, sediment properties and
907 sedimentation patterns. Basin Research, 17(3), 383-402.
908 <https://doi.org/10.1111/j.1365-2117.2005.00274.x>

909 Gradmann, S., Beaumont, C., & Albertz, M., (2009). Factors controlling the evolution
910 of the Perdido Fold Belt, northwestern Gulf of Mexico, determined from numerical
911 models. Tectonics, 28(2). <https://doi.org/10.1029/2008TC002326>

912 Gradmann, S., & Beaumont, C., (2016). Numerical modelling study of mechanisms
913 of mid-basin salt canopy evolution and their potential applications to the
914 Northwestern Gulf of Mexico. Basin Research 29(4), 490-520.
915 <https://doi.org/10.1111/bre.12186>

916 Hardy, S., & Finch, E., (2005). Discrete-element modelling of detachment
917 folding. *Basin Research*, 17(4), 507-520. <https://doi.org/10.1111/j.1365->
918 [2117.2005.00280.x](https://doi.org/10.1111/j.1365-2117.2005.00280.x)

919 Hardy, S., Finch, E., (2006). Discrete element modelling of the influence of cover
920 strength on basement-involved fault-propagation folding. *Tectonophysics*, 415, 225-
921 238. <https://doi.org/10.1016/j.tecto.2006.01.002>

922 Hardy, S., & Finch, E., (2007). Mechanical stratigraphy and the transition from
923 trishear to kink-band fault-propagation fold forms above blind basement thrust faults:
924 a discrete-element study. *Marine and Petroleum Geology*, 24(2), 75-90.
925 <https://doi.org/10.1016/j.marpetgeo.2006.09.001>

926 Hudec, M. R., & Jackson, M. P., (2004). Regional restoration across the Kwanza
927 Basin, Angola: Salt tectonics triggered by repeated uplift of a metastable passive
928 margin. *AAPG Bulletin*, 88(7), 971-990. <https://doi.org/10.1306/02050403061>

929 Hudec, M. R., & Jackson, M. P., (2007). Terra infirma: Understanding salt
930 tectonics. *Earth-Science Reviews*, 82(1), 1-28.
931 <https://doi.org/10.1016/j.earscirev.2007.01.001>

932 Hudec, M. R., Norton, I. O., Jackson, M. P., & Peel, F. J., (2013). Jurassic evolution
933 of the Gulf of Mexico salt basin. *AAPG Bulletin*, 97(10), 1683-1710.
934 <https://doi.org/10.1306/04011312073>

935 Ings, S. J., & Shimeld, J. W. (2006). A new conceptual model for the structural
936 evolution of a regional salt detachment on the northeast Scotian margin, offshore
937 eastern Canada. *AAPG Bulletin*, 90(9), 1407-1423.
938 <https://doi.org/10.1306/04050605159>

939 Jackson, C. A. L., Jackson, M. P., & Hudec, M. R., (2015). Understanding the
940 kinematics of salt-bearing passive margins: A critical test of competing hypotheses
941 for the origin of the Albian Gap, Santos Basin, offshore Brazil. *Geological Society of
942 America Bulletin*, 127(11-12), 1730-1751. <https://doi.org/10.1130/B31290.1>

943 Jackson, C. A. L., Jackson, M. P., Hudec, M. R., & Rodriguez, C. R., (2015).
944 Enigmatic structures within salt walls of the Santos Basin—Part 1: Geometry and
945 kinematics from 3D seismic reflection and well data. *Journal of Structural
946 Geology*, 75, 135-162. <https://doi.org/10.1016/j.jsg.2015.01.010>

947 Jackson, M. P., Hudec, M. R., Jennette, D. C., & Kilby, R. E., (2008). Evolution of the
948 Cretaceous Astrid thrust belt in the ultradeep-water Lower Congo Basin, Gabon.
949 *AAPG Bulletin*, 92(4), 487-511. <https://doi.org/10.1306/12030707074>

950 Jackson, M. P., & Hudec, M. R., (2017). *Salt Tectonics: Principles and Practice*.
951 Cambridge University Press. <https://doi.org/10.1017/9781139003988>

952 Johnson, R. B., & DeGraff, J. V., (1988). *Principles of engineering geology*. Wiley.

953 Li, S. Y., & Urai, J. L., (2016). Rheology of rock salt for salt tectonics modeling.
954 *Petroleum Science*, 13(4), 712-724.

955 Liang, W. G., Yang, C. H., Zhao, Y. S., Dusseault, M. B., & Liu, J., (2007).
956 Experimental investigation of mechanical properties of bedded salt rock.
957 *International Journal of Rock Mechanics and Mining Sciences*, 44(3), 400-411.
958 <https://doi.org/10.1016/j.ijrmms.2006.09.007>

959 Mitchell, N. C., Ligi, M., Ferrante, V., Bonatti, E., & Rutter, E., (2010). Submarine salt
960 flows in the central Red Sea. *GSA Bulletin*, 122(5-6), 701-713.
961 <https://doi.org/10.1130/B26518.1> Mohriak, W.U., Macedo, J.M., Castellani, R.T.,

962 Rangel, H.D., Barros, A.Z.N., Latgé, M.A.L., Mizusaki, A.M.P., Szatmari, P.,
963 Demercian, L.S., Rizzo, J.G., & Aires, J.R., (1995). Salt tectonics and structural
964 styles in the deep-water province of the Cabo Frio region, Rio de Janeiro, Brazil. in
965 M. P. A. Jackson, D. G. Roberts, and S. Snelson, eds., Salt tectonics: a global
966 perspective: AAPG Memoir 65, 273-304.

967 Mora, P., & Place, D., (1993). A lattice solid model for the nonlinear dynamics of
968 earthquakes. *International Journal of Modern Physics C*, 4(06), 1059-1074.
969 <https://doi.org/10.1306/M65604C13>

970 Mora, P., & Place, D., (1994). Simulation of the frictional stick-slip instability. *Pure*
971 *and applied geophysics*, 143(1-3), 61-87. <https://doi.org/10.1007/BF00874324>

972 Peel, F. J. (2014). The engines of gravity-driven movement on passive margins:
973 Quantifying the relative contribution of spreading vs. gravity sliding
974 mechanisms. *Tectonophysics*, 633, 126-142.
975 <https://doi.org/10.1016/j.tecto.2014.06.023>

976 Pichel, L. M., Finch, E., Huuse, M., & Redfern, J., (2017). The influence of shortening
977 and sedimentation on rejuvenation of salt diapirs: A new Discrete-Element Modelling
978 approach. *Journal of Structural Geology*, 104, 61-79.

979 Pichel, L.M., Peel, F., Jackson, C.A.-L., Huuse, M., 2018, Geometry and kinematics
980 of salt-detached ramp syncline basins, *Journal of Structural Geology*, 115, 208-230. ,
981 doi: 10.1016/ j.jsjg.2018.07.016.

982 Place, D., Lombard, F., Mora, P., & Abe, S., (2002). Simulation of the micro-physics
983 of rocks using LSMearth. In *Earthquake Processes: Physical Modelling, Numerical*

984 Simulation and Data Analysis Part I (pp. 1911-1932). Birkhäuser Basel.
985 <https://doi.org/10.1007/s00024-002-8715-x>

986 Quirk, D. G., Schødt, N., Lassen, B., Ings, S. J., Hsu, D., Hirsch, K. K., & Von
987 Nicolai, C., (2012). Salt tectonics on passive margins: examples from Santos,
988 Campos and Kwanza basins. Geological Society, London, Special Publications, 363,
989 207-244. <https://doi.org/10.1144/SP363.10>

990 Rowan, M. G., (1995). Structural styles
991 and evolution of allochthonous salt, central Louisiana outer shelf and upper slope, in
992 M. P. A. Jackson, D. G. Roberts, and S. Snelson, eds., Salt tectonics: a global
993 perspective: AAPG Memoir 65, 199-228. <https://doi.org/10.1306/M65604C9>

994 Rowan, M. G., Trudgill, B. D., & Carl Fiduk, J., (2000). Deep-Water, Salt-Cored
995 Foldbelts: Lessons from the Mississippi Fan and Perdido Foldbelts, Northern Gulf of
996 Mexico. Atlantic rifts and continental margins, 173-191. *Geophysical Monograph-*
American Geophysical Union, 115, 173-192. <https://doi.org/10.1029/GM115p0173>

997 Rowan, M. G., Peel, F. J., & Vendeville, B. C., (2004). Gravity-driven fold belts on
998 passive margins. In: McKlay, K.R. (Ed.) Thrust tectonics and Hydrocarbon Systems.
999 AAPG Memoir 82, 157-182. <https://doi.org/10.1306/M82813C9>

1000 Rowan, M. G. (2014). Passive-margin salt basins: hyperextension, evaporite
1001 deposition, and salt tectonics. *Basin Research*, 26(1), 154-182.
1002 <https://doi.org/10.1111/bre.12043>

1003 Schöpfer, M. P. J., Childs, C. & Walsh, J. J., (2006). Localisation of normal faults in
1004 multilayer sequences. *Journal of Structural Geology*, 28, 816-833.
1005 <https://doi.org/10.1016/j.jsg.2006.02.003>

1006 Schultz-Ela, D. D., Jackson, M. P., & Vendeville, B. C., (1993). Mechanics of active
1007 salt diapirism. *Tectonophysics*, 228(3-4), 275-312. [https://doi.org/10.1016/0040-](https://doi.org/10.1016/0040-1951(93)90345-K)
1008 1951(93)90345-K

1009 Spiers, C. J., Schutjens, P. M. T. M., Brzesowsky, R. H., Peach, C. J., Liezenberg, J.
1010 L., & Zwart, H. J., (1990). Experimental determination of constitutive parameters
1011 governing creep of rocksalt by pressure solution. Geological Society, London,
1012 Special Publications, 54, 215-227. <https://doi.org/10.1144/GSL.SP.1990.054.01.21>

1013 Tari, G., Molnar, J., Ashton, P., & Hedley, R., (2000). Salt tectonics in the Atlantic
1014 margin of Morocco. *The Leading Edge*, 19(10), 1074-1078.
1015 <https://doi.org/10.1190/1.1438481>

1016 Tari, G., Molnar, J., & Ashton, P., (2003). Examples of salt tectonics from West
1017 Africa: a comparative approach. Geological Society, London, Special
1018 Publications, 207, 85-104. <https://doi.org/10.1144/GSL.SP.2003.207.5>

1019 Tari, G., & Jabour, H., (2013). Salt tectonics along the Atlantic margin of
1020 Morocco. Geological Society, London, Special Publications, 369, 337-353.
1021 <https://doi.org/10.1144/SP369.23>

1022 Tari, G., Novotny, B., Jabour, H., & Hafid, M., (2017). Salt tectonics along the
1023 Atlantic Margin of NW Africa (Morocco and Mauritania). In: Soto, J. I., Flinch, J., &
1024 Tari, G. (Eds.). (2017). *Permo-Triassic Salt Provinces of Europe, North Africa and*
1025 *the Atlantic Margins: Tectonics and Hydrocarbon Potential*. Elsevier, 331-351.
1026 <https://doi.org/10.1016/B978-0-12-809417-4.00016-1>

1027 Vendeville, B. C., & Jackson, M. P. A., (1992). The rise of diapirs during thin-skinned
1028 extension. *Marine and Petroleum Geology*, 9(4), 331-354.
1029 [https://doi.org/10.1016/0264-8172\(92\)90047-I](https://doi.org/10.1016/0264-8172(92)90047-I)

1030 Vendeville, B. C., Ge, H., & Jackson, M. P. A., (1995). Scale models of salt tectonics
1031 during basement-involved extension. *Petroleum Geoscience*, 1(2), 179-183.
1032 <https://doi.org/10.1144/petgeo.1.2.179>

1033 Wagner, B. H., & Jackson, M. P., (2011). Viscous flow during salt welding.
1034 *Tectonophysics*, 510(3), 309-326. <https://doi.org/10.1016/j.tecto.2011.07.012>

1035 Weijermars, R., & Schmeling, H., (1986). Scaling of Newtonian and non-Newtonian
1036 fluid dynamics without inertia for quantitative modelling of rock flow due to gravity
1037 (including the concept of rheological similarity). *Physics of the Earth and Planetary*
1038 *Interiors*, 43(4), 316-330. [https://doi.org/10.1016/0031-9201\(86\)90021-X](https://doi.org/10.1016/0031-9201(86)90021-X)

1039 Weijermars, R., Jackson, M. T., & Vendeville, B., (1993). Rheological and tectonic
1040 modeling of salt provinces. *Tectonophysics*, 217(1-2), 143-174.
1041 [https://doi.org/10.1016/0040-1951\(93\)90208-2](https://doi.org/10.1016/0040-1951(93)90208-2)

1042 Weijermars, R., Hudec, M. R., Dooley, T. P., & Jackson, M. P. A., (2015).
1043 Downbuilding salt stocks and sheets quantified in 3-D analytical models. *Journal of*
1044 *Geophysical Research: Solid Earth*, 120(6), 4616-4644.
1045 <https://doi.org/10.1002/2014JB011704>